

Multipath Extended Target Tracking with Labeled Random Finite Sets

Guanhua Ding, *Student Member, IEEE*, Tao Huang, *Senior Member, IEEE*, Qinchen Wu, *Student Member, IEEE*, Jinping Sun, *Member, IEEE*, Yanping Wang, *Member, IEEE*, Bing Zhu, *Senior Member, IEEE*, and Guoqiang Mao, *Fellow, IEEE*

Abstract—High-resolution radar sensors are critical for autonomous systems but pose significant challenges to traditional tracking algorithms due to the generation of multiple measurements per object and the presence of multipath effects. Existing solutions often rely on the point target assumption or treat multipath measurements as clutter, whereas current extended target trackers often lack the capability to maintain trajectory continuity in complex multipath environments. To address these limitations, this paper proposes the multipath extended target generalized labeled multi-Bernoulli (MPET-GLMB) filter. A unified Bayesian framework based on labeled random finite set theory is derived to jointly model target existence, measurement partitioning, and the association between measurements, targets, and propagation paths. This formulation enables simultaneous trajectory estimation for both targets and reflectors without requiring heuristic post-processing. To enhance computational efficiency, a joint prediction and update implementation based on Gibbs sampling is developed. Furthermore, a measurement-driven adaptive birth model is introduced to initialize tracks without prior knowledge of target positions. Experimental results from simulated scenarios and real-world automotive radar data demonstrate that the proposed filter outperforms state-of-the-art methods, achieving superior state estimation accuracy and robust trajectory maintenance in dynamic multipath environments.

Index Terms—Multi-target tracking, radar multipath effect, extended target tracking, labeled random finite sets.

I. INTRODUCTION

MULTIPLE target tracking (MTT) is a fundamental task in autonomous driving, intelligent transportation, and robotics. Traditional MTT formulations rely on the *point target* assumption, which states that each target generates at most

This work has been submitted to the IEEE for possible publication. Copyright may be transferred without notice, after which this version may no longer be accessible. The work of Guanhua Ding, Qinchen Wu, and Jinping Sun was supported by the National Natural Science Foundation of China under Grants 62131001 and 62171029. The work of Bing Zhu was supported by the National Natural Science Foundation of China, Grant 62573019. (Corresponding author: Jinping Sun.)

Guanhua Ding, Qinchen Wu, and Jinping Sun are with the School of Electronic Information Engineering, Beihang University, Beijing 100191, China (e-mail: buaadgh@buaa.edu.cn, wuqinchen@buaa.edu.cn, sunjinping@buaa.edu.cn).

Tao Huang is with the College of Science and Engineering, James Cook University, Cairns, QLD 4870, Australia (e-mail: tao.huang1@jcu.edu.au).

Yanping Wang is with the School of Artificial Intelligence and Computer Science, North China University of Technology, Beijing 100144, China (e-mail: wangyp@ncut.edu.cn).

Bing Zhu is with the School of Automation Science and Electrical Engineering, Beihang University, Beijing 100191, China (e-mail: zhubing@buaa.edu.cn).

Guoqiang Mao is with Research Laboratory of Smart Driving and Intelligent Transportation Systems, Southeast University, Nanjing 210096, China (e-mail: g.mao@ieee.org).

one measurement per sensor scan. This assumption underlies classical MTT algorithms, including global nearest neighbor (GNN) [1], joint probabilistic data association (JPDA) [2], multiple hypothesis tracking (MHT) [3], and random finite set (RFS)-based filters [4], [5], [6]. With the advent of high-resolution sensors such as LiDAR and mmWave radar, the point-target assumption has become largely invalid. When the target physical dimensions exceed the sensor's resolution, reflections arise from multiple scattering centers, producing clusters of measurements rather than single points. This necessitates joint estimation of target centroid kinematics and spatial extent (size and orientation), motivating the development of multiple *extended target* tracking (METT) methods. Various extended target models, including the random matrix [7], [8], [9], [10], random hypersurface [11], Gaussian process [12], and probabilistic measurement-region association [13], have been explored for radar- and LiDAR-based METT.

When radar sensors operate in geometrically complex environments, such as urban streets and indoor warehouses, the free-space line-of-sight (LOS) propagation assumption is frequently violated. Electromagnetic waves may reflect off static structures, such as buildings and fences, before returning to the receiver, resulting in multipath propagation that creates *ghost targets* at virtual locations. These effects pose significant challenges for data association and track management.

A straightforward approach to mitigate multipath effects is to suppress multipath return signals through antenna design and signal processing [14], [15] or discard ghost measurements using gating [1] or machine learning-based identification methods [16], [17]. However, these approaches discard valuable information contained in multipath measurements. In scenarios where the direct LOS path is occluded, multipath reflections may provide the only evidence of a target's presence [18]. Consequently, recent studies have sought to exploit multipath measurements as non-line-of-sight (NLOS) information rather than discarding them. Several multi-detection (MD) tracking methods based on conventional JPDA and MHT filters have been developed for over-the-horizon radar (OTHR) and underwater sonar multipath propagation models [19], [20], [21]. Yang et al. proposed the MP-GLMB filter based on the generalized labeled multi-Bernoulli (GLMB) RFS for OTHR multipath tracking [22], followed by a more efficient Gibbs sampling-based implementation in [23]. These methods, however, rely on accurate prior knowledge of the multipath propagation model, which is often unavailable in dynamic traffic and indoor sensing environments. A joint target-tracking and

wall-estimation method was proposed in [24], where multipath measurements are identified using a Hough transform-based ghost recognition algorithm and unknown wall parameters are estimated via an extended Kalman filter (EKF). Nevertheless, all the aforementioned methods assume point targets and are therefore unsuitable for high-resolution radar sensors.

For extended targets tracking with multipath measurements, the MP-RM-PDA filter [25] adopts random matrix modeling and explicitly enumerates possible multipath association events within a probabilistic data association framework, resulting in high computational complexity and requiring well-separated targets with known cardinality *a priori*. The MP-ET-RFS tracker [26] employs a two-stage strategy, using a probability hypothesis density (PHD) filter to pre-process measurements, followed by a multipath Bernoulli filter for final estimation. Although this design reduces computational cost, the lack of explicit extent estimation can degrade tracking performance. The MP-ET-PHD filter [27] provides a state-of-the-art RFS-based solution that jointly estimates the kinematic state and spatial extent of an unknown number of targets using multipath measurements. However, as a PHD-based method, it produces only unlabeled state estimates, preventing direct trajectory extraction without heuristic post-processing and often leading to unstable cardinality estimates [28]. Moreover, these RFS-based methods generally rely on precise prior knowledge of multipath propagation models, which limits their applicability in complex and dynamic environments.

This study proposes the multipath extended target generalized labeled multi-Bernoulli (MPET-GLMB) filter, a unified Bayesian framework designed to address the aforementioned limitations. To the best of our knowledge, this is the first work to effectively integrate a labeled RFS formulation with extended target models in dynamic multipath environments. The main contributions of this work are summarized as follows:

- A GLMB recursion is derived that jointly accounts for uncertainties in target existence, measurement partitioning, and measurement–target–path association. It enables simultaneous trajectory estimation of both targets and reflectors, providing a closed-form solution to multiple extended target tracking in multipath environments.
- A Gibbs sampling-based joint prediction and update implementation of the MPET-GLMB filter is developed, eliminating inefficient truncation procedures and resulting in a computationally tractable solution.
- A measurement-driven adaptive birth model is proposed for robust trajectory initialization that identifies potential reflectors with Hough transform and automatically determines the parameters of newborn targets.
- A comprehensive evaluation is conducted, in which the MPET-GLMB filter is benchmarked against the state-of-the-art MP-ET-PHD filter using both simulated and real-world radar data. The results demonstrate the superior state estimation accuracy and trajectory continuity of the proposed method in dynamic multipath environments.

The remainder of this paper is organized as follows. Section II provides background on the radar multipath propagation model and labeled RFS-based tracking. Section III presents

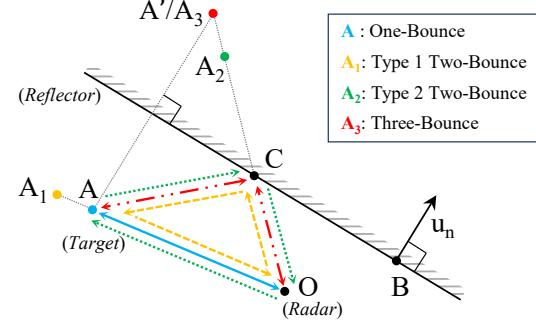


Fig. 1. Radar multipath propagation geometry.

the mathematical derivation of the proposed MPET-GLMB filter, and Section IV describes its efficient implementation. Experimental results and analysis are reported in Section V. Finally, conclusions are drawn in Section VI.

II. BACKGROUND

A. Radar Multipath Propagation Model

According to standard extended target measurement models, each target measurement originates from a scattering center distributed on the target's spatial extent [7], [29], [30]. Therefore, defining a multipath propagation model for point targets provides the basis for solving the METT problem.

Consider the geometry illustrated in Fig. 1, where a radar located at $O = [o_x, o_y]^T$ observes a target at $A = [a_x, a_y]^T$ with respective velocities $v^O = [v_x^O, v_y^O]^T$ and $v^A = [v_x^A, v_y^A]^T$. The signal is reflected at a specular point $C = [c_x, c_y]^T$ on a stationary reflective surface \mathcal{S} , resulting in multipath effects. Without loss of generality, the reflective surface \mathcal{S} is modeled as a line characterized by a point $B = [b_x, b_y]^T$ and a unit normal vector $u_n = [u_x, u_y]^T$. As shown in Fig. 1, the mirrored target A' and its velocity $v^{A'}$ are given by

$$A' = A - \overrightarrow{AA'} = A - 2(\overrightarrow{BA} \cdot u_n)u_n,$$

$$v^{A'} = dA'/dt = v^A - 2(v^A \cdot u_n)u_n,$$

where $p \cdot q$ denotes the dot product, $\overrightarrow{pq} \triangleq q - p$, and $d(\cdot)/dt$ denotes the time derivative.

The specular point C is the intersection of the ray $\overrightarrow{OA'}$ and the reflective surface \mathcal{S} . Let $u_t = [-u_y, u_x]^T$ be the unit tangent vector of \mathcal{S} . The point C is obtained by solving $B + s_1 u_t = O + s_2 \overrightarrow{OA'}$ for scalars s_1 and s_2 . Eliminating s_2 yields

$$s_1 = -(\overrightarrow{OA'} * \overrightarrow{OB}) / (\overrightarrow{OA'} * u_t),$$

where $p * q \triangleq p_x q_y - p_y q_x$. The specular point is then given by $C = B + s_1 u_t$.

With the above model, four propagation paths are identified:

- Direct path (one-bounce) \mathfrak{P}_0 : $O \rightarrow A \rightarrow O$;
- Type 1 two-bounce path \mathfrak{P}_1 : $O \rightarrow C \rightarrow A \rightarrow O$;
- Type 2 two-bounce path \mathfrak{P}_2 : $O \rightarrow A \rightarrow C \rightarrow O$;
- Three-bounce path \mathfrak{P}_3 : $O \rightarrow C \rightarrow A \rightarrow C \rightarrow O$.

Higher-order multipath effects caused by multiple reflective surfaces are not considered in this study.

Assume that the radar measures range r , azimuth ϕ , and Doppler velocity \dot{r} . For the direct propagation path \mathfrak{P}_0 , the ideal measurement $z_0 = [r_0, \phi_0, \dot{r}_0]^T$ is given by:

$$z_0 = \left[\|\overrightarrow{OA}\|, \angle(\overrightarrow{OA}), (v^A - v^O) \cdot \left(\overrightarrow{OA} / \|\overrightarrow{OA}\| \right) \right]^T,$$

where $\|\cdot\|$ denotes the Euclidean norm, and $\angle(\overrightarrow{OA})$ returns the angle between \overrightarrow{OA} and the x-axis.

The three-bounce propagation path \mathfrak{P}_3 is geometrically equivalent to a direct path toward the mirrored target A' . Accordingly, its ideal measurement z_3 is obtained by substituting A and v^A in z_0 with A' and $v^{A'}$, respectively. For the two-bounce paths \mathfrak{P}_1 and \mathfrak{P}_2 , the range and Doppler are averaged over the \mathfrak{P}_0 and \mathfrak{P}_3 paths [24]. Consequently, the path \mathfrak{P}_1 generates a ghost target A_1 sharing the azimuth of A , while \mathfrak{P}_2 creates a ghost target A_2 sharing the azimuth of A' . The ideal measurements are given by

$$z_1 = [(r_0 + r_3)/2, \phi_0, (\dot{r}_0 + \dot{r}_3)/2]^T, \quad z_2 = [r_1, \phi_3, \dot{r}_1]^T.$$

B. Multi-Target Tracking with Labeled RFS

RFS-based multi-target Bayes filtering provides a flexible and rigorous framework for estimating the states of multiple targets from noisy measurements [31]. Rather than modeling each target's state individually, the multi-target state is represented as a finite set, enabling principled handling of missed detections, false alarms (clutter), and unknown data association. Labeled RFSs [32] are widely adopted in MTT, as the labels allow online trajectory estimation without heuristic post-processing. Following conventional notation, unlabeled vectors and scalars are denoted by lower case letters (e.g., x). Unlabeled sets and matrices are in upper case (e.g., X). Labeled states and densities are in boldface (e.g., \mathbf{x} , \mathbf{X} , and $\boldsymbol{\pi}$). The multi-target exponential of a function is given by $h^X \triangleq \prod_{x \in X} h(x)$, with $h^\emptyset = 1$. The inner product is denoted by $\langle f, g \rangle \triangleq \int f(x)g(x)dx$. The generalized Kronecker delta and the inclusion function are defined as:

$$\delta_Y(X) = \begin{cases} 1 & \text{if } X = Y \\ 0 & \text{otherwise} \end{cases}, \quad 1_Y(X) = \begin{cases} 1 & \text{if } X \subseteq Y \\ 0 & \text{otherwise} \end{cases}.$$

Definition 1: A labeled RFS \mathbf{X} on the state space \mathbb{X} and label space \mathbb{L} consists of elements with distinct labels [32]. With the label projection $\mathcal{L}(x, \ell) = \ell$, the distinct label indicator is defined by $\Delta(\mathbf{X}) = \delta_{|\mathbf{X}|}(|\mathcal{L}(\mathbf{X})|)$, where $|\mathbf{X}|$ denotes set cardinality and $\mathcal{L}(\mathbf{X})$ is the set of labels in \mathbf{X} .

At time k , the multi-object state \mathbf{X}_k is partially observed through a set of measurements $Z_k \subset \mathbb{Z}$. The measurement history is denoted as $Z_{1:k-1} = (Z_1, \dots, Z_{k-1})$. Given the prior density $\boldsymbol{\pi}_{k-1}(\mathbf{X}_{k-1} | Z_{1:k-1})$, the prediction density is computed via the Chapman–Kolmogorov equation [32]

$$\begin{aligned} \boldsymbol{\pi}_{k|k-1}(\mathbf{X}_k | Z_{1:k-1}) \\ = \int f_{k|k-1}(\mathbf{X}_k | \mathbf{X}_{k-1}) \boldsymbol{\pi}_{k-1}(\mathbf{X}_{k-1} | Z_{1:k-1}) \delta \mathbf{X}_{k-1}. \end{aligned} \quad (1)$$

where $f_{k|k-1}(\mathbf{X}_k | \mathbf{X}_{k-1})$ is the multi-target transition kernel. The posterior density is obtained using Bayes' rule

$$\boldsymbol{\pi}_k(\mathbf{X}_k | Z_{1:k}) = \frac{\boldsymbol{\pi}_{k|k-1}(\mathbf{X}_k | Z_{1:k-1}) g_k(Z_k | \mathbf{X}_k)}{\int \boldsymbol{\pi}_{k|k-1}(\mathbf{X}_k | Z_{1:k-1}) g_k(Z_k | \mathbf{X}_k) \delta \mathbf{X}_k}. \quad (2)$$

where $g_k(Z_k | \mathbf{X}_k)$ denotes the multi-target likelihood. Labeled target states can be extracted directly from the resulting posterior density. For notational simplicity, the time index k and the conditioning on past measurements are omitted hereafter, and the subscript $k|k-1$ is abbreviated as $+$.

A conjugate prior is required in multi-target Bayes filtering to obtain closed-form solutions to (1) and (2). The GLMB density is a conjugate prior widely used in labeled RFS-based trackers [29], [33], [34], [35].

Definition 2: A GLMB RFS \mathbf{X} on $\mathbb{X} \times \mathbb{L}$ has density

$$\boldsymbol{\pi}(\mathbf{X}) = \Delta(\mathbf{X}) \sum_{c \in \mathbb{C}} w^{(c)}(\mathcal{L}(\mathbf{X})) [p^{(c)}]^{\mathbf{X}},$$

where \mathbb{C} is a discrete index set [29]. The weights satisfy $\sum_{J \subseteq \mathbb{L}} \sum_{c \in \mathbb{C}} w^{(c)}(J) = 1$, and each single-target densities satisfy $\int_{x \in \mathbb{X}} p^{(c)}(x, \ell) dx = 1$.

Definition 3: A δ -GLMB RFS \mathbf{X} on $\mathbb{X} \times \mathbb{L}$ is a special case of the GLMB with

$$\begin{aligned} \mathbb{C} &= \mathcal{F}(\mathbb{L}) \times \Xi, \quad p^{(c)} = p^{(I, \xi)} = p^{(\xi)}, \\ w^{(c)}(J) &= w^{(I, \xi)}(J) = w^{(I, \xi)} \delta_I(J), \end{aligned}$$

where $\mathcal{F}(\mathbb{L})$ denotes the set of all finite subsets of \mathbb{L} , and Ξ denotes a discrete space [32]. The resulting density is:

$$\boldsymbol{\pi}(\mathbf{X}) = \Delta(\mathbf{X}) \sum_{I \in \mathcal{F}(\mathbb{L}), \xi \in \Xi} w^{(I, \xi)} \delta_I(\mathcal{L}(\mathbf{X})) [p^{(\xi)}]^{\mathbf{X}}. \quad (3)$$

Each hypothesis (I, ξ) consists of a label set I and an association history ξ . The weight $w^{(I, \xi)}$ denotes the probability of this hypothesis, and $p^{(\xi)}(x, \ell)$ is the single-target density.

Existing GLMB filters address point targets with known multipath propagation models [22] but do not handle extended targets with dynamic multipath effects. In following sections, we derive a δ -GLMB-based Bayesian filtering recursion for METT with dynamic multipath observations, and present an efficient implementation of the proposed filter.

III. METT WITH DYNAMIC MULTIPATH OBSERVATIONS

A. Observation Model of Multiple Extended Targets

Conditioned on the multi-target state \mathbf{X} and the measurement set Z , the multi-target likelihood $g(Z | \mathbf{X})$ is derived under the following assumptions:

- A1.** A target with state $\mathbf{x} \in \mathbf{X}$ is detected via the direct path \mathfrak{P}_0 with probability $P_d(\mathbf{x})$. Its detection probability via path $\mathfrak{P}_{m \in M = \{1, 2, 3\}}$ is $P_{d,R}(\mathbf{x}, \mathbf{x}^*, m)$, where $\mathbf{x}^* \in \mathbf{X}$ is the state of another target providing the reflective surface. The misdetection probabilities are $q_d(\mathbf{x}) = 1 - P_d(\mathbf{x})$ and $q_{d,R}(\mathbf{x}, \mathbf{x}^*, m) = 1 - P_{d,R}(\mathbf{x}, \mathbf{x}^*, m)$, respectively.
- A2.** If detected via \mathfrak{P}_0 , the target generates measurements $W \subseteq Z$ with likelihood $\tilde{g}_D(W | \mathbf{x})$. If detected via \mathfrak{P}_m , the likelihood is $\tilde{g}_R(W | \mathbf{x}, \mathbf{x}^*, m)$.
- A3.** Clutter is modeled as an independent Poisson RFS with intensity $\kappa(\cdot)$. For a clutter set C , the likelihood is $g_c(C) = e^{-\int \kappa(z) dz} \kappa^C$ [33].

By enumerating all multi-bounce propagation paths, the set of multi-bounce target state tuples is

$$\mathbf{T}(\mathbf{X}, M) = \{(\mathbf{x}_i, \mathbf{x}_j, m) : i, j \in \mathcal{L}(\mathbf{X}), i \neq j, m \in M\},$$

where each tuple $\mathbf{t} \in \mathbf{T}(\mathbf{X}, M)$ is uniquely labeled by $\rho = (i, j, m)$ with label projection $\mathcal{L}(t, \rho) = \rho$.

Let $\mathcal{P}^S(Z)$ denote the set of all partitions that separate Z into exactly S non-empty subsets. For a partition $\mathcal{U} = \{\mathcal{U}_1, \dots, \mathcal{U}_S\} \in \mathcal{P}^S(Z)$, let $\Theta_{\mathbf{X}, \mathbf{T}}^{\mathcal{U}}$ denote the set of admissible association mappings (θ, φ) , where $\theta : \mathcal{L}(\mathbf{X}) \rightarrow \{0, \dots, |\mathcal{U}|\}$ denotes the direct path association and $\varphi : \mathcal{L}(\mathbf{T}(\mathbf{X}, M)) \rightarrow \{0, \dots, |\mathcal{U}|\}$ is the multi-bounce path association. Validity requires that all non-zero assignments are unique and mutually disjoint, i.e., $\theta(\ell) \neq \varphi(\rho)$ whenever $\theta(\ell) > 0$ and $\varphi(\rho) > 0$.

Proposition 1: The multi-target measurement likelihood is:

$$g(Z|\mathbf{X}) = g_c(Z) \sum_{\substack{S=1, \dots, \mathcal{S}(\mathbf{X}, M)+1 \\ \mathcal{U} \in \mathcal{P}^S(Z), (\theta, \varphi) \in \Theta_{\mathbf{X}, \mathbf{T}}^{\mathcal{U}}}} [\Psi_{D, \mathcal{U}}^{(\theta)}]^{\mathbf{X}} [\Psi_{R, \mathcal{U}}^{(\varphi)}]^{\mathbf{T}(\mathbf{X}, M)}. \quad (4)$$

Here, $\mathcal{S}(\mathbf{X}, M) = |\mathbf{X}| + |\mathbf{X}|(|\mathbf{X}| - 1)|M|$ is the total number of possible propagation paths. The functions $\Psi_{D, \mathcal{U}}^{(\theta)}(\mathbf{x}) \triangleq \psi_{D, \mathcal{U}}^{(\theta(\mathcal{L}(\mathbf{x})))}(\mathbf{x})$, $\Psi_{R, \mathcal{U}}^{(\varphi)}(\mathbf{t}) \triangleq \psi_{R, \mathcal{U}}^{(\varphi(\mathcal{L}(\mathbf{t})))}(\mathbf{t})$ correspond to direct path and multi-bounce path associations, respectively. The component likelihoods are:

$$\psi_{D, \mathcal{U}}^{(s)}(\mathbf{x}) = \begin{cases} \frac{P_d(\mathbf{x}) \tilde{g}_D(\mathcal{U}_s | \mathbf{x})}{\kappa^{\mathcal{U}_s}} & \text{if } s \in \{1, \dots, |\mathcal{U}|\} \\ q_d(\mathbf{x}) & \text{if } s = 0 \end{cases}, \quad (5a)$$

$$\psi_{R, \mathcal{U}}^{(s)}(\mathbf{t}) = \begin{cases} \frac{P_{d,R}(\mathbf{t}) \tilde{g}_R(\mathcal{U}_s | \mathbf{t})}{\kappa^{\mathcal{U}_s}} & \text{if } s \in \{1, \dots, |\mathcal{U}|\} \\ q_{d,R}(\mathbf{t}) & \text{if } s = 0 \end{cases}. \quad (5b)$$

Proof: Separate the measurement set into disjoint subsets

$$\mathcal{U}^*(Z) = \{C, Y_n, B_\rho : n \in \mathcal{L}(\mathbf{X}), \rho \in \mathcal{L}(\mathbf{T}), \uplus_{\mathcal{U}^*(Z)} = Z\},$$

where C denotes the clutter, Y_n is the direct-path measurement set generated by target \mathbf{x}_n , and $B_{\rho=(i,j,m)}$ is the multi-bounce measurement set of target \mathbf{x}_i via propagation path \mathfrak{P}_m , with target \mathbf{x}_j acting as the reflector. Notably, $\mathcal{U}^*(Z)$ is not a partition of Z , as it may contain empty subsets. Under Assumptions A1–A3, the multi-target likelihood is written as a sum over all realizations of $\mathcal{U}^*(Z)$:

$$g(Z|\mathbf{X}) = \sum_{\mathcal{U}^*(Z)} g_c(C) \prod_{n, \rho} g_D(Y_n | \mathbf{x}_n) g_R(B_\rho | \mathbf{t}_\rho), \quad (6)$$

where $n \in \mathcal{L}(\mathbf{X})$ and $\rho \in \mathcal{L}(\mathbf{T})$, with

$$\begin{aligned} g_D(Y|\mathbf{x}) &= \begin{cases} P_d(\mathbf{x}) \tilde{g}_D(Y|\mathbf{x}) & \text{if } Y \neq \emptyset \\ q_d(\mathbf{x}) & \text{if } Y = \emptyset \end{cases}, \\ g_R(B|\mathbf{t}) &= \begin{cases} P_{d,R}(\mathbf{t}) \tilde{g}_R(B|\mathbf{t}) & \text{if } B \neq \emptyset \\ q_{d,R}(\mathbf{t}) & \text{if } B = \emptyset \end{cases}. \end{aligned}$$

Separating the empty and non-empty subsets of $\mathcal{U}^*(Z)$ yields

$$\begin{aligned} g(Z|\mathbf{X}) &= \sum_{C \uplus W = Z} g_c(C) [q_d]^{\mathbf{X}} [q_{d,R}]^{\mathbf{T}(\mathbf{X}, M)} \sum_{\substack{S=1, \dots, \mathcal{S}(\mathbf{X}, M) \\ \mathcal{U} \in \mathcal{P}^S(W), (\theta, \varphi) \in \Theta_{\mathbf{X}, \mathbf{T}}^{\mathcal{U}}}} \\ &\quad \times \prod_{\theta(n) > 0} \frac{P_d(\mathbf{x}_n) \tilde{g}_D(\mathcal{U}_{\theta(n)} | \mathbf{x}_n)}{q_d(\mathbf{x}_n)} \prod_{\varphi(\rho) > 0} \frac{P_{d,R}(\mathbf{t}_\rho) \tilde{g}_R(\mathcal{U}_{\varphi(\rho)} | \mathbf{t}_\rho)}{q_{d,R}(\mathbf{t}_\rho)}. \end{aligned}$$

Since $C = Z - W$, the clutter can be absorbed into the measurement partition, resulting in

$$g(Z|\mathbf{X}) = g_c(Z) [q_d]^{\mathbf{X}} [q_{d,R}]^{\mathbf{T}(\mathbf{X}, M)} \sum_{\substack{S=1, \dots, \mathcal{S}(\mathbf{X}, M)+1 \\ \mathcal{U} \in \mathcal{P}^S(Z), (\theta, \varphi) \in \Theta_{\mathbf{X}, \mathbf{T}}^{\mathcal{U}}}}$$

$$\times \prod_{\theta(n) > 0} \frac{P_d(\mathbf{x}_n) \tilde{g}_D(\mathcal{U}_{\theta(n)} | \mathbf{x}_n)}{q_d(\mathbf{x}_n) \kappa^{\mathcal{U}_{\theta(n)}}} \prod_{\varphi(\rho) > 0} \frac{P_{d,R}(\mathbf{t}_\rho) \tilde{g}_R(\mathcal{U}_{\varphi(\rho)} | \mathbf{t}_\rho)}{q_{d,R}(\mathbf{t}_\rho) \kappa^{\mathcal{U}_{\varphi(\rho)}}}.$$

Finally, by multiplying $[q_d^d]^{\mathbf{X}}$ and $[q_R^d]^{\mathbf{T}(\mathbf{X}, M)}$ into the summation, the misdetection terms in the denominators cancel out, yielding the likelihood expression in (4).

B. δ -GLMB Filtering Recursion

Consider a δ -GLMB multi-target prior density of the form (3) and a newborn target state \mathbf{X}_B with density [32]

$$\Delta(\mathbf{X}_B) [1_{\mathbb{B}_+} r_{B+}]^{\mathcal{L}(\mathbf{X}_B)} [1 - r_{B+}]^{\mathbb{B}_+ - \mathcal{L}(\mathbf{X}_B)} [p_{B+}]^{\mathbf{X}_B}, \quad (7)$$

where \mathbb{B}_+ is the label space of newborn targets, $r_{B+}(\ell)$ is the birth probability of a target labeled by ℓ , and $p_{B+}(x, \ell)$ is the corresponding single-target state density.

Conditioned on \mathbf{X} , each target $\mathbf{x} \in \mathbf{X}$ survives independently with probability $P_S(\mathbf{x})$ and transitions according to $f_+(\mathbf{x}_+ | \mathbf{x})$. Under these assumptions, the δ -GLMB prediction density is given by [36]:

$$\pi_+(\mathbf{X}) = \Delta(\mathbf{X}) \sum_{\xi \in \Xi, I_+ \in \mathcal{F}(\mathbb{L} \uplus \mathbb{B}_+)} w_+^{(I_+, \xi)} \delta_{I_+}(\mathcal{L}(\mathbf{X})) [\bar{p}_+^{(\xi)}]^{\mathbf{X}}, \quad (8)$$

where

$$w_+^{(I_+, \xi)} = [1_{\mathbb{B}_+} r_{B+}]^{I_+ \cap \mathbb{B}_+} [1 - r_{B+}]^{\mathbb{B}_+ - I_+} \sum_{I \in \mathcal{F}(\mathbb{L})} \quad (9a)$$

$$\times \mathcal{I}_{\mathcal{F}(I)}(I_+ \cap I) [\bar{P}_S^{(\xi)}]^{I_+ \cap I} [1 - \bar{P}_S^{(\xi)}]^{I - I_+} w^{(I, \xi)} \quad (9b)$$

$$\begin{aligned} \bar{p}_+^{(\xi)}(\mathbf{x}_+) &= \mathcal{I}_{\mathbb{B}_+}(\ell_+) p_{B+}(\mathbf{x}_+) + \mathcal{I}_{\mathbb{L}}(\ell_+) \\ &\quad \times \langle p^{(\xi)}(\cdot, \ell_+), P_S(\cdot, \ell_+) f_+(x_+ | \cdot, \ell_+) \rangle / \bar{P}_S^{(\xi)}(\ell_+) \end{aligned} \quad (9c)$$

With the prediction density (8) and likelihood (4), we have

$$\begin{aligned} \pi_+(\mathbf{X}) g(Z|\mathbf{X}) &= g_c(Z) \Delta(\mathbf{X}) \sum_{\xi, I_+, S, \mathcal{U}, \theta, \varphi} w_+^{(I_+, \xi)} \delta_{I_+}(\mathcal{L}(\mathbf{X})) \\ &\quad \times [\bar{p}_+^{(\xi)} \Psi_{D, \mathcal{U}}^{(\theta)}]^{\mathbf{X}} [\Psi_{R, \mathcal{U}}^{(\varphi)}]^{\mathbf{T}(\mathbf{X}, M)}, \end{aligned}$$

where $(\xi, I_+) \in \Xi \times \mathcal{F}(\mathbb{L} \uplus \mathbb{B}_+)$, $S = 1, \dots, \mathcal{S}(\mathbf{X}, M) + 1$, $\mathcal{U} \in \mathcal{P}^S(Z)$, $(\theta, \varphi) \in \Theta_{\mathbf{X}, \mathbf{T}}^{\mathcal{U}}$. Since $[\Psi_{R, \mathcal{U}}^{(\varphi)}]^{\mathbf{T}(\mathbf{X}, M)}$ is not a multi-target exponential for \mathbf{X} , the posterior density $\pi(\mathbf{X}|Z) \propto \pi_+(\mathbf{X}) g(Z|\mathbf{X})$ does not belong to the δ -GLMB family, and approximations are thus required to restore conjugacy.

In traffic environments, reflective surfaces, such as walls and guardrails, exhibit distinct shapes, sizes, and motion characteristics that differ fundamentally from those of pedestrians and vehicles. Accordingly, separate state models are adopted for objects and reflectors, and the multi-target state is partitioned as $\mathbf{X} = \mathbf{X}^o \uplus \mathbf{X}^r$, where $\mathbf{x}^o \in \mathbf{X}^o$ denotes the state of an object and $\mathbf{x}^r \in \mathbf{X}^r$ is the state of a reflector. By neglecting multipath interactions among objects, the set of valid multi-bounce tuples reduces to $\tilde{\mathbf{T}}(\mathbf{X}, M) = \{(\mathbf{x}_i, \mathbf{x}_j^r, m) : i \in \mathcal{L}(\mathbf{X}), j \in \mathcal{L}(\mathbf{X}^r), i \neq j, m \in M\} = \{\tilde{\mathbf{t}}_\rho\}$. Under these assumptions, the multi-target likelihood becomes

$$g(Z|\mathbf{X}) = g_c(Z) \sum_{S, \mathcal{U}, \theta, \varphi} [\Psi_{D, \mathcal{U}}^{(\theta)}]^{\mathbf{X}} [\Psi_{R, \mathcal{U}}^{(\varphi)}]^{\tilde{\mathbf{T}}(\mathbf{X}, M)}, \quad (10)$$

where $S = 1, \dots, \mathcal{S}^*(\mathbf{X}, M) + 1$, $\mathcal{S}^*(\mathbf{X}, M) = |\mathbf{X}| + |\mathbf{X}^r|(|\mathbf{X}| - 1)|M|$ is the number of admissible propagation paths, $\mathcal{U} \in \mathcal{P}^S(Z)$, and $(\theta, \varphi) \in \Theta_{\mathbf{X}, \tilde{\mathbf{T}}}^{\mathcal{U}}$.

Furthermore, to obtain a δ -GLMB posterior, the function $\hat{\psi}_{R, \mathcal{U}}^{(s)}(\mathbf{t})$ in (5b), defined for $\mathbf{t} = (\mathbf{x}_i, \mathbf{x}_j, m)$, is approximated by a function depending only on the target state \mathbf{x}_i :

$$\hat{\psi}_{R, \mathcal{U}}^{(s, j, m)}(\mathbf{x}_i) = \begin{cases} \frac{\hat{P}_{d, R}^{(j, m)}(\mathbf{x}_i) \hat{g}_R^{(j, m)}(\mathcal{U}_s | \mathbf{x}_i)}{\kappa_{\mathcal{U}_s}} & \text{if } s \in \{1, \dots, |\mathcal{U}|\}, \\ \hat{q}_{d, R}^{(j, m)}(\mathbf{x}_i) & \text{if } s = 0, \end{cases} \quad (11)$$

where $\hat{g}_R^{(j, m)}(\mathcal{U}_s | \mathbf{x}_i) \triangleq \tilde{g}_R(\mathcal{U}_s | \mathbf{x}_i, \hat{\mathbf{x}}_j^r, m)$, $\hat{P}_{d, R}^{(j, m)}(\mathbf{x}_i) \triangleq P_{d, R}(\mathbf{x}_i, \hat{\mathbf{x}}_j^r, m)$, and $\hat{q}_{d, R}^{(j, m)}(\mathbf{x}_i) = 1 - \hat{P}_{d, R}^{(j, m)}(\mathbf{x}_i)$. Here, the estimated reflector state set $\hat{\mathbf{X}}^r$ is treated as a fixed parameter, removing the explicit dependence on \mathbf{x}_j^r . Substituting (11) into (10), the multi-target likelihood is approximated by

$$\hat{g}(Z | \mathbf{X}) = g_c(Z) \sum_{\substack{S=1, \dots, \mathcal{S}^*(\mathbf{X}, M) + 1 \\ \mathcal{U} \in \mathcal{P}^S(Z), (\theta, \varphi) \in \Theta_{\mathbf{X}, \tilde{\mathbf{T}}}^{\mathcal{U}}}} [\hat{\Psi}_{\mathcal{U}}^{(\theta, \varphi)}]^{\mathbf{X}}, \quad (12)$$

where

$$\hat{\Psi}_{\mathcal{U}}^{(\theta, \varphi)}(\mathbf{x}) = \psi_{D, \mathcal{U}}^{(\theta, \ell)}(\mathbf{x}) \prod_{j \in \mathcal{L}(\hat{\mathbf{X}}^r) - \{\ell\}, m \in M} \hat{\psi}_{R, \mathcal{U}}^{(\varphi, \ell, j, m), j, m}(\mathbf{x}). \quad (13)$$

Proposition 2: Given the predicted δ -GLMB density in (8) and the approximated multi-target likelihood in (12), the posterior multi-target density is a δ -GLMB of the form

$$\pi(\mathbf{X} | Z) = \Delta(\mathbf{X}) \sum_{\xi, I_+, S, \mathcal{U}, \theta, \varphi} w_{\mathcal{U}}^{(I_+, \xi, \theta, \varphi)} \delta_{I_+}(\mathcal{L}(\mathbf{X})) [p_{\mathcal{U}}^{(\xi, \theta, \varphi)}]^{\mathbf{X}} \quad (14)$$

where $(\xi, I_+) \in \Xi \times \mathcal{F}(\mathbb{L} \uplus \mathbb{B}_+)$, $S = 1, \dots, \mathcal{S}^*(\mathbf{X}, M) + 1$, $\mathcal{U} \in \mathcal{P}^S(Z)$, $(\theta, \varphi) \in \Theta_{\mathbf{X}, \tilde{\mathbf{T}}}^{\mathcal{U}}$. The component weights and single-target posteriors are given by

$$w_{\mathcal{U}}^{(I_+, \xi, \theta, \varphi)} \propto w_{+}^{(I_+, \xi)} [\eta_{\mathcal{U}}^{(\xi, \theta, \varphi)}]^{I_+}, \quad (15a)$$

$$p_{\mathcal{U}}^{(\xi, \theta, \varphi)}(x, \ell) = \bar{p}_+^{(\xi)}(x, \ell) \hat{\Psi}_{\mathcal{U}}^{(\theta, \varphi)}(x, \ell) / \eta_{\mathcal{U}}^{(\xi, \theta, \varphi)}(\ell), \quad (15b)$$

$$\eta_{\mathcal{U}}^{(\xi, \theta, \varphi)}(\ell) = \int \bar{p}_+^{(\xi)}(x, \ell) \hat{\Psi}_{\mathcal{U}}^{(\theta, \varphi)}(x, \ell) dx. \quad (15c)$$

Proof: The product of the prediction density $\pi_+(\mathbf{X})$ and the approximated likelihood $\hat{g}(Z | \mathbf{X})$ is

$$\begin{aligned} & \pi_+(\mathbf{X}) \hat{g}(Z | \mathbf{X}) \\ &= g_c(Z) \Delta(\mathbf{X}) \sum_{\xi, I_+, S, \mathcal{U}, \theta, \varphi} w_{+}^{(I_+, \xi)} \delta_{I_+}(\mathcal{L}(\mathbf{X})) [\bar{p}_+^{(\xi)} \hat{\Psi}_{\mathcal{U}}^{(\theta, \varphi)}]^{\mathbf{X}} \\ &= g_c(Z) \Delta(\mathbf{X}) \sum_{\xi, I_+, S, \mathcal{U}, \theta, \varphi} w_{+}^{(I_+, \xi)} \delta_{I_+}(\mathcal{L}(\mathbf{X})) [\eta_{\mathcal{U}}^{(\xi, \theta, \varphi)}]^{\mathcal{L}(\mathbf{X})} \\ & \quad \times [p_{\mathcal{U}}^{(\xi, \theta, \varphi)}(\cdot)]^{\mathbf{X}} \\ &= g_c(Z) \Delta(\mathbf{X}) \sum_{\xi, I_+, S, \mathcal{U}, \theta, \varphi} w_{+}^{(I_+, \xi)} [\eta_{\mathcal{U}}^{(\xi, \theta, \varphi)}]^{I_+} \delta_{I_+}(\mathcal{L}(\mathbf{X})) [p_{\mathcal{U}}^{(\xi, \theta, \varphi)}]^{\mathbf{X}}. \end{aligned}$$

The normalizing factor is given by the set integral

$$\begin{aligned} & \int \pi_+(\mathbf{X}) \hat{g}(Z | \mathbf{X}) \delta \mathbf{X} \\ &= g_c(Z) \sum_{\xi, I_+} w_{+}^{(I_+, \xi)} \int \Delta(\mathbf{X}) \delta_{I_+}(\mathcal{L}(\mathbf{X})) \sum_{S, \mathcal{U}, \theta, \varphi} \\ & \quad \times [\bar{p}_+^{(\xi)}(\cdot) \hat{\Psi}_{\mathcal{U}}^{(\theta, \varphi)}(\cdot)]^{\mathbf{X}} \delta \mathbf{X} \end{aligned}$$

$$\begin{aligned} &= g_c(Z) \sum_{\xi, I_+} w_{+}^{(I_+, \xi)} \sum_{L \subseteq \mathbb{L} \uplus \mathbb{B}_+} \delta_{I_+}(L) \sum_{S, \mathcal{U}, \theta, \varphi} \\ & \quad \times \left[\int \bar{p}_+^{(\xi)}(x, \cdot) \hat{\Psi}_{\mathcal{U}}^{(\theta, \varphi)}(x, \cdot) dx \right]^L \\ &= g_c(Z) \sum_{\xi, I_+} w_{+}^{(I_+, \xi)} \sum_{S, \mathcal{U}, \theta, \varphi} [\eta_{\mathcal{U}}^{(\xi, \theta, \varphi)}]^{I_+}, \end{aligned}$$

where Lemma 3 in [32] is applied. Substituting the above results into Bayes' rule (2) yields the posterior density (14).

C. Extended Target Modeling

In this study, the object states are modeled by the gamma Gaussian inverse Wishart (GGIW) density [29], [37], while reflectors are represented by a uniform stick model.

1) *GGIW Model:* Let W denote the set of measurements generated by an object with state $x = (x_\gamma, x_K, x_E)$. Under the GGIW model, the number of measurements follows a Poisson distribution $\mathcal{PS}(|W|; x_\gamma)$. Poisson rate $x_\gamma > 0$ follows a gamma distribution with probability density function (PDF)

$$\mathcal{G}(x_\gamma; \alpha, \beta) = \frac{\beta^\alpha}{\Gamma(\alpha)} x_\gamma^{\alpha-1} e^{-\beta x_\gamma},$$

where $\alpha > 0$ is the shape parameter, and $\beta > 0$ is the rate parameter. The kinematic state $x_K = [p_x, p_y, v_x, v_y]^T \in \mathbb{R}^4$ is modeled as a Gaussian distribution $\mathcal{N}(x_K; \mu, P)$ with mean μ and covariance P . The spatial extent is represented by a symmetric positive definite matrix $x_E \in \mathbb{S}^2$, which follows an inverse Wishart distribution

$$\mathcal{IW}(x_E; \nu, V) = \frac{|V|^{\frac{\nu}{2}} |x_E|^{-\frac{(\nu+3)}{2}}}{2^\nu \Gamma_2(\frac{\nu}{2})} e^{-\text{tr}(V x_E^{-1})/2},$$

where $\nu > 1$ is the degrees of freedom, $V \in \mathbb{S}^2$ is the scale matrix, $\Gamma_2(\cdot)$ is the multi-variate gamma function, and $\text{tr}(\cdot)$ denotes the matrix trace. Combining the definitions above, the object state density is given by [29]:

$$\begin{aligned} p(x) &= \mathcal{G}(x_\gamma; \alpha, \beta) \mathcal{N}(x_K; \mu, P) \mathcal{IW}(x_E; \nu, V) \\ &= \mathcal{GGIW}(x; \chi) \end{aligned} \quad (16)$$

where $\chi = (\alpha, \beta, \mu, P, \nu, V)$ is the set of GGIW parameters.

The kinematic state transition density is modeled as

$$f_+(x_{K+} | x_K) = \mathcal{N}(x_{K+}; F_+ x_K, G_+ Q_+ G_+^T). \quad (17)$$

The near-constant-velocity motion model [38] is adopted in this study, while other maneuver models can also be applied under the formulation of (17). The state transition matrix F_+ , process noise covariance Q_+ , and noise gain matrix G_+ are:

$$\begin{aligned} F_+ &= \begin{bmatrix} 1 & \tau_+ \\ 0 & 1 \end{bmatrix} \otimes \text{diag}(1, 1), \quad Q_+ = \text{diag}(\sigma_x^2, \sigma_y^2), \\ G_+ &= [\tau_+^2/2, \tau_+]^T \otimes \text{diag}(1, 1), \end{aligned}$$

where \otimes denotes the Kronecker product, τ_+ is the time interval, and $\text{diag}(\cdot)$ returns a diagonal matrix. Following [29], [30], [39], the predicted density $p_+(x)$ is approximated as $\mathcal{GGIW}(x; \chi_+)$ with parameters

$$\begin{aligned} \alpha_+ &= \alpha/\epsilon, \quad \beta_+ = \beta/\epsilon, \quad \mu_+ = F_+ \mu, \quad P_+ = F_+ P F_+^T + Q_+, \\ \nu_+ &= e^{-\tau_+/\tau_0} (\nu + 3) - 3, \quad V_+ = V \nu_+ / \nu. \end{aligned}$$

Here, ϵ is an exponential forgetting factor, where a larger ϵ increases the variance of x_γ . Similarly, τ_0 is a temporal decay factor, where a larger τ_0 results in a smaller variance in x_E .

2) *Uniform Stick Model*: The GGIW model, which assumes elliptical extents, is unsuitable for long stick-shaped reflectors. Therefore, a spatial distribution-based extent representation [13], [40] is adopted, and reflectors are modeled as uniform sticks. Consider a reflector with state $x = (x_\gamma, x_K, x_E)$. The Poisson rate x_γ and the kinematic state x_K are modeled identically to those of objects. The extent state is instead defined as $x_E = [\mathfrak{h}, \mathfrak{s}, \mathfrak{e}]^T \in \mathbb{R}^3$, where \mathfrak{h} denotes the heading angle, and $(\mathfrak{s}, \mathfrak{e})$ are the scalar offsets of the starting and ending points along the reflector. Given the centroid position $C_0 = [p_x, p_y]^T$ and the extent state x_E of a reflector, the endpoints are computed as

$$C_{\text{start}} = C_0 + \mathfrak{s} \begin{bmatrix} \cos(\mathfrak{h}) \\ \sin(\mathfrak{h}) \end{bmatrix}, \quad C_{\text{end}} = C_0 + \mathfrak{e} \begin{bmatrix} \cos(\mathfrak{h}) \\ \sin(\mathfrak{h}) \end{bmatrix}. \quad (18)$$

The extent state transition density is modeled as

$$f_+(x_{E+}|x_E) = \mathcal{N}(x_{E+}; x_E, Q_{E+}), \quad (19)$$

where $Q_{E+} = \text{diag}(\sigma_{\mathfrak{h}}^2, \sigma_{\mathfrak{s}}^2, \sigma_{\mathfrak{e}}^2)$ represents the process noise covariance matrix.

D. Multipath Measurement Model

Consider an extended target with state $x = (x_\gamma, x_K, x_E)$ generating a set of measurements W . The likelihood function is $\tilde{g}(W|x) = \mathcal{PS}(|W|; x_\gamma) \prod_{z \in W} p(z|x)$ [29], [39]. Each measurement $z \in W$ originates from a reflective point with state $\check{x} = [\check{p}_x, \check{p}_y, \check{v}_x, \check{v}_y]^T$. Following Section II-A, the measurement model under propagation path \mathfrak{P}_m is

$$z = [r, \phi, \dot{r}]^T = \begin{cases} h_m(\check{x}, x_O) + \omega & m = 0, \\ h_m(\check{x}, x_O, x^*) + \omega & m \in \{1, 2, 3\}, \end{cases}$$

where $h_m(\cdot)$ is the nonlinear measurement function, x_O is the radar state, and x^* denotes the reflector state. The measurement noise $\omega = [\omega_r, \omega_\phi, \omega_{\dot{r}}]^T \sim \mathcal{N}(0, \tilde{R})$ has covariance matrix $\tilde{R} = \text{diag}(\sigma_r^2, \sigma_\phi^2, \sigma_{\dot{r}}^2)$. As discussed in Section III-B, the estimated reflector state $\hat{x}^* \in \hat{X}^r$ is used to parameterize the reflective surface \mathfrak{S} . The nonlinear measurement function is denoted by $\hat{h}_m(\cdot)$ for brevity.

Assuming reflective points are uniformly distributed over the target extent and share the centroid velocity, the single-measurement likelihood is

$$p(z|x) = \int p(z|\check{x}, x)p(\check{x}|x)d\check{x} = \mathcal{N}(\dot{r}; \hat{h}_m^r(x_K), \sigma_{\dot{r}}^2) \times \int \mathcal{N}(z^{r\phi}; \hat{h}_m^{r\phi}(\check{x}^p), \text{diag}(\sigma_r^2, \sigma_\phi^2)) \mathcal{U}\mathcal{N}(\check{x}^p; x)d\check{x}^p, \quad (20)$$

where superscripts select vector components (e.g., $z^{r\phi} = [r, \phi]^T$ denotes the range–azimuth measurement vector), and $\mathcal{U}\mathcal{N}(\cdot)$ is the uniform density over the target extent.

E. GGIW Update for Objects

For GGIW-modeled objects, the elliptical uniform distribution of reflective points is approximated by a Gaussian PDF $\mathcal{N}(\check{x}^p; x_K^p, \varrho x_E)$ with scaling parameter $\varrho = 1/4$ [7]. Approximating $\hat{h}_m(\cdot)$ by its first-order Taylor series expansion around the object centroid yields the Jacobian matrix $H_m = \partial \hat{h}_m / \partial x_K|_{x_K=\hat{x}_K}$, and the likelihood is computed as

$$p(z|x) \approx \mathcal{N}(z; \hat{h}_m(x_K), R_m(x_E)). \quad (21)$$

The covariance matrix accounts for both measurement noise and object's extent, given by

$$R_m(x_E) = \text{diag}(\varrho \check{H}_m x_E \check{H}_m^T + \text{diag}(\sigma_r^2, \sigma_\phi^2, \sigma_{\dot{r}}^2)), \quad (22)$$

where \check{H}_m denotes the upper-left 2×2 sub-matrix of H_m .

When an object generates a set of measurements W via propagation path \mathfrak{P}_m , a Poisson rate scaling factor γ_m is introduced to model path-dependent attenuation with $\gamma_0 = 1$ for the direct path and $\gamma_m \in (0, 1]$ for multi-bounce paths. The corresponding likelihood is

$$\tilde{g}(W|x) = \mathcal{PS}(|W|; \gamma_m x_\gamma) \prod_{z \in W} \mathcal{N}(z; \hat{h}_m(x_K), R_m(x_E)).$$

Given the predicted GGIW density $p_+(x) = \mathcal{GGIW}(x; \chi_+)$, the posterior density $p(x|W)$ is computed via Bayes' rule. The unnormalized posterior is

$$\tilde{p}(x|W) = \mathcal{G}(x_\gamma; \alpha_+, \beta_+) \mathcal{N}(x_K; \mu_+, P_+) \mathcal{IW}(x_E; \nu_+, V_+) \times \mathcal{PS}(|W|; \gamma_m x_\gamma) \prod_{z \in W} \mathcal{N}(z; \hat{h}_m(x_K), R_m(x_E)). \quad (23)$$

Following [29], [41], [42] and Appendix A, the posterior $p(x|W)$ is approximated by $\mathcal{GGIW}(x; \chi_W)$ with updated parameters:

$$\begin{aligned} \alpha_W &= \alpha_+ + |W|, & \beta_W &= \beta_+ + \gamma_m, \\ \mu_W &= \mu_+ + K(\bar{z} - h_m(\mu_+)), & P_W &= P_+ - K \Lambda K^T, \\ \nu_W &= \nu_+ + |W| - 1, & V_W &= V_+ + \check{H}_m^{-1} \check{D} (\check{H}_m^{-1})^T / \varrho. \end{aligned}$$

Here, \bar{z} is the centroid of W , $K = P_+ H_m^T \Lambda^{-1}$ is the Kalman gain, $\Lambda = H_m P_+ H_m^T + R_m(\bar{E})/|W|$ is the innovation covariance calculated using the expected extent $\bar{E} = V_+ / (\nu_+ - 3)$, and \check{D} is the upper-left 2×2 submatrix of the scatter matrix $D = \sum_{z \in W} (z - \bar{z})(z - \bar{z})^T$.

The marginal likelihood required for the GLMB update is

$$\int p_+(x) \tilde{g}(W|x) dx = \eta_\gamma \eta_z \eta_R^{\frac{1-|W|}{2}} \eta_{IW} \quad (24)$$

with components

$$\begin{aligned} \eta_\gamma &= \frac{\beta^\alpha \Gamma(\alpha + |W|) \gamma_m^{|W|}}{\Gamma(\alpha) (\beta + \gamma_m)^{(\alpha + |W|)} |W|!}, & \eta_z &= \mathcal{N}(\bar{z}; \hat{h}_m(\mu_+), \Lambda), \\ \eta_R &= (\sigma_r^2 \sigma_\phi^2 \sigma_{\dot{r}}^2) |\bar{E}^{-1} + \varrho \check{H}_m^T \text{diag}(\sigma_r^{-2}, \sigma_\phi^{-2}) \check{H}_m|, \\ \eta_{IW} &= \frac{(2\pi)^{\frac{3(1-|W|)}{2}} 2^{|W|-1} |V_+|^{\frac{\nu_+}{2}} \Gamma_2(\frac{\nu_W}{2})}{|V_W|^{\frac{\nu_W}{2}} \Gamma_2(\frac{\nu_+}{2})} e^{\text{tr}(D\Omega)/2}, \end{aligned}$$

where $\Omega = \text{diag}(\bar{E}^{-1} \text{diag}(\sigma_r^2, \sigma_\phi^2) \bar{E}^{-1}, -\sigma_{\dot{r}}^{-2})$, and $\bar{E} = \varrho \check{H}_m \bar{E} \check{H}_m^T$. This formulation shows that when a prior GGIW density $p_+(x)$ is updated by multiple measurement sets as

in (15), and the object detection probabilities in (11) are independent of x , the resulting posterior $p_{\mathcal{U}(Z)}^{(\xi, \theta, \varphi)}(x, \ell)$ remains a GGIW density.

F. Particle Update for Reflectors

For reflectors modeled by the uniform stick representation, the gamma parameters (α, β) of the measurement rate x_γ are updated using the closed-form expressions in Section III-E, whereas the kinematic and extent states require a different update strategy. Reflective points \tilde{x} are assumed to be uniformly distributed along the line segment defined by the endpoints in (18). Accordingly, the position of a reflective point is expressed as $\tilde{x}_c^p = x_K^p + cu_t(\mathfrak{h})$, where c is uniformly distributed on $[\mathfrak{s}, \mathfrak{e}]$, and $u_t(\mathfrak{h}) = [\cos(\mathfrak{h}), \sin(\mathfrak{h})]^T$ is the unit tangent vector. The corresponding unit normal vector is $u_n(\mathfrak{h}) = [-\sin(\mathfrak{h}), \cos(\mathfrak{h})]^T$. Consequently, the likelihood (20) becomes

$$\begin{aligned} p(z|x) &= \mathcal{N}(\dot{r}; \hat{h}_m^r(x_K), \sigma_r^2) \\ &\quad \times \frac{1}{\mathfrak{e} - \mathfrak{s}} \int_{\mathfrak{s}}^{\mathfrak{e}} \mathcal{N}(z^{r\phi}; \hat{h}_m^{r\phi}(\tilde{x}_c^p), \text{diag}(\sigma_r^2, \sigma_\phi^2)) dc. \end{aligned} \quad (25)$$

Since this integral has no closed-form solution, and the elliptical Gaussian approximation in (21) is inaccurate over the reflector's spatial extent, particle filtering is adopted to estimate the kinematic and extent states of reflectors.

First, (25) is approximated by a closed-form expression to enable efficient particle weight updates [8], [13]. The Gaussian integral is approximated in Cartesian coordinates as

$$\int_{\mathfrak{s}}^{\mathfrak{e}} \mathcal{N}(\dots) dc \approx \int_{\mathfrak{s}}^{\mathfrak{e}} \mathcal{N}(z_{xy}; \tilde{x}_c^p, R_{xy}) dc,$$

where the Cartesian measurement position is obtained via the inverse measurement function $z_{xy} = \hat{h}_m^{-1}(z^{r\phi})$, and the approximated covariance is $R_{xy} = \hat{H}_m^{-1} \text{diag}(\sigma_r^2, \sigma_\phi^2) (\hat{H}_m^{-1})^T$. Assuming the reflector extent is significantly larger than the measurement noise standard deviation, the multivariate Gaussian can be further approximated by two independent Gaussian components [8]:

$$\begin{aligned} \int_{\mathfrak{s}}^{\mathfrak{e}} \mathcal{N}(z_{xy}; \tilde{x}_c^p, R_{xy}) dc &\approx \mathcal{N}(d_z; 0, \sigma_n^2) \int_{\mathfrak{s}}^{\mathfrak{e}} \mathcal{N}(c; \mu_t, \sigma_t^2) dc \\ &= \mathcal{N}(d_z; 0, \sigma_n^2) \left[Q\left(\frac{\mathfrak{s} - \mu_t}{\sigma_t}\right) - Q\left(\frac{\mathfrak{e} - \mu_t}{\sigma_t}\right) \right], \end{aligned} \quad (26)$$

where $Q(\cdot)$ denotes the Q-function [43], and

$$\begin{aligned} d_z &= |u_n(\mathfrak{h}) \cdot \Delta z|, \quad \sigma_n^2 = u_n(\mathfrak{h})^T R_{xy} u_n(\mathfrak{h}), \\ \mu_t &= u_t(\mathfrak{h}) \cdot \Delta z, \quad \sigma_t^2 = u_t(\mathfrak{h})^T R_{xy} u_t(\mathfrak{h}). \end{aligned} \quad (27)$$

Here, $\Delta z = h_m^{-1}(z^{r\phi}) - x_K^p$, d_z denotes the distance between z_{xy} and the reflector, μ_t is the projection of Δz on the reflector, and σ_n^2 and σ_t^2 are the projected noise variance along the normal and tangent directions, respectively [8]. As a result, the likelihood (25) yields a closed-form approximation.

Next, the prior kinematic and extent states are represented by a set of particles $\mathcal{X}_- = \{(x_{K-}^{(l)}, x_{E-}^{(l)}, \lambda_-^{(l)})\}_{l=1}^L$ with weights satisfying $\sum_n \lambda_-^{(l)} = 1$. Predicted particles \mathcal{X}_+ are sampled from the transition densities (17) and (19), i.e.,

$$x_{K+}^{(l)} \sim \mathcal{N}(F_+ x_{K-}^{(l)}, G_+ Q_+ G_+^T), \quad x_{E+}^{(l)} \sim \mathcal{N}(x_{E-}^{(l)}, Q_{E+}),$$

and $\lambda_+^{(l)} = \lambda_-^{(l)}$. When the reflector is detected via path \mathfrak{P}_m with measurements W , particle weights are sequentially updated. Assume that the measurements are indexed in an arbitrary order as $W = \{z^{(\zeta)}\}_{\zeta=1}^{|W|}$. For the ζ -th measurement, the weights are updated as $\lambda^{(l, \zeta)} = \tilde{\lambda}_+^{(l, \zeta)} / \sum_{l=1}^L \tilde{\lambda}_+^{(l, \zeta)}$, where

$$\begin{aligned} \tilde{\lambda}_+^{(l, \zeta)} &= \lambda_+^{(l, \zeta-1)} \mathcal{N}(\dot{r}^{(\zeta)}; \hat{h}_m^r(x_{K+}^{(l)}), \sigma_r^2) \\ &\quad \times \frac{\mathcal{N}(d_z; 0, \sigma_n^2)}{\mathfrak{e}_+^{(l)} - \mathfrak{s}_+^{(l)}} \left[Q\left(\frac{\mathfrak{s}_+^{(l)} - \mu_t}{\sigma_t}\right) - Q\left(\frac{\mathfrak{e}_+^{(l)} - \mu_t}{\sigma_t}\right) \right]. \end{aligned}$$

Quantities $(d_z, \sigma_n^2, \mu_t, \sigma_t^2)$ are calculated by substituting $z^{(\zeta)}$, $x_{K+}^{(l)}$, and $x_{E+}^{(l)}$ into (27). Process all measurements to obtain the updated particles $\mathcal{X} = \{(x_K^{(l, |W|)}, x_E^{(l, |W|)}, \lambda^{(l, |W|)})\}_{l=1}^L$. To mitigate weight degeneracy, systematic resampling with a Metropolis-Hastings step [44] is applied to the updated particles when the number of effective particles falls below a threshold, i.e., $1 / \sum_l (\lambda^{(l, |W|)})^2 < L_{\text{eff}}$. Finally, the marginal likelihood is approximated by $\prod_{\zeta=1}^{|W|} \sum_{l=1}^L \tilde{\lambda}_+^{(l, \zeta)}$ [13], [44].

IV. EFFICIENT FILTER IMPLEMENTATION

This section details the implementation and pseudocode of the proposed MPET-GLMB filter.

A. δ -GLMB Joint Prediction and Update

The separated δ -GLMB prediction and update recursion in Section III-B computes the prediction density $\pi_+(\mathbf{X})$ independently of the measurements, which typically results in a large number of low-weight GLMB components and requires inefficient intermediate truncation [36]. To mitigate this issue, the joint prediction and update strategy in [45] is adopted, in which target birth, death, and survival events are jointly enumerated together with measurement associations. By substituting the predicted weights in (9a) into (15a), the joint posterior density is obtained as

$$\begin{aligned} \pi(\mathbf{X}|Z) &\propto \Delta(\mathbf{X}) \sum_{\xi, I, I_+, S, \mathcal{U}, \theta, \varphi} w^{(I, \xi)} \\ &\quad \times w_{\mathcal{U}}^{(I, I_+, \xi, \theta, \varphi)} \delta_{I_+}(\mathcal{L}(\mathbf{X})) [p_{\mathcal{U}}^{(\xi, \theta, \varphi)}] \mathbf{X}, \end{aligned} \quad (28)$$

where the joint weight accounts for target birth and survival probabilities with measurement likelihoods is

$$\begin{aligned} w_{\mathcal{U}(Z)}^{(I, I_+, \xi, \theta, \varphi)} &= [1_{\mathbb{B}_+} r_{\mathbb{B}_+}]^{I_+ \cap \mathbb{B}_+} [1 - r_{\mathbb{B}_+}]^{\mathbb{B}_+ - I_+} \\ &\quad \times [\bar{P}_S^{(\xi)}]^{I_+ \cap I} [1 - \bar{P}_S^{(\xi)}]^{I - I_+} [\eta_{\mathcal{U}(Z)}^{(\xi, \theta, \varphi)}]^{I_+}, \end{aligned} \quad (29)$$

since (15a) can be rewritten as

$$w_{\mathcal{U}}^{(I_+, \xi, \theta, \varphi)} \propto w_+^{(I_+, \xi)} [\eta_{\mathcal{U}}^{(\xi, \theta, \varphi)}]^{I_+} = \sum_{I \in \mathcal{F}(\mathbb{L})} w^{(I, \xi)} w_{\mathcal{U}}^{(I, I_+, \xi, \theta, \varphi)}.$$

The posterior (28) indicates that each prior GLMB component (I, ξ) generates a set of child components $(I, \xi, I_+, \theta, \varphi)$ during the joint prediction and update step. As the number of components grows exponentially, truncation is performed at each time step by retaining only those with the largest weights, which minimizes the L_1 approximation error [32].

Given a GLMB component (I, ξ) and a measurement partition $\mathcal{U} = \{\mathcal{U}_1, \dots, \mathcal{U}_S\}$, the target labels are enumerated as

$$I = I^o \uplus I^r = \{\ell_1 : \ell_{N_I^o}\} \uplus \{\ell_{N_I^o+1} : \ell_{N_I}\},$$

$$\mathbb{B}_+ = \mathbb{B}_+^o \uplus \mathbb{B}_+^r = \{\ell_{N_I+1} : \ell_{N_B^o}\} \uplus \{\ell_{N_B^o+1} : \ell_N\}.$$

Here, I^o and I^r denote the label sets of existing objects and reflectors, respectively. The label sets of newborn objects and reflectors are denoted by \mathbb{B}_+^o and \mathbb{B}_+^r , respectively. The number of reflectors is given by $N^r = N_I - N_I^o + N - N_B^o$.

For each $(I_+, \theta, \varphi) \in \mathcal{F}(\mathbb{L} \uplus \mathbb{B}_+) \times \Theta_{\mathbf{X}, \tilde{\mathbf{T}}}^{\mathcal{U}}$, a unified association matrix ϑ of size $N \times (3N^r + 1)$ is introduced:

$$\vartheta_{i,j} = \begin{cases} \theta(\ell_i) & \text{if } j = 1, \ell_i \in I_+, \\ \varphi((\ell_i, \ell_{j^*}, m)) & \text{if } j > 1, \ell_i \in I_+, \ell_i \neq \ell_{j^*}, \\ 0 & \text{if } j > 1, \ell_i \in I_+, \ell_i = \ell_{j^*}, \\ -1 & \text{otherwise,} \end{cases} \quad (30)$$

where $m = \lceil (j-1)/N^r \rceil$ ($\lceil \cdot \rceil$ is the ceiling function) identifies the propagation path, and $j^* = N_I^o + j - (m-1)N^r - 1$ indexes the reflector. In this representation, $\vartheta_{i,j} = -1$ signifies target death or non-existence, $\vartheta_{i,j} = 0$ indicates target existence without detection, and $\vartheta_{i,j} > 0$ denotes an association between the target and a specific measurement subset.

If a target ℓ_i exists ($\vartheta_{i,1} \geq 0$) but its multi-bounce path (ℓ_i, ℓ_{j^*}, m) can not be established, the corresponding entry in (30) is still set to $\vartheta_{i,j} = 0$, which is equivalent to an existing path with zero detection probability. If a target does not exist, none of its multi-bounce paths can exist. Consequently, the i -th row of ϑ satisfies $\vartheta_i \in \mathbb{E} \uplus \mathbb{N}$, where $\mathbb{E} = \{0 : S\}^{3N^r+1}$ represents target existence and $\mathbb{N} = \{-1\}^{3N^r+1}$ represents target extinction.

With this definition, ϑ inherits the one-to-one (1-1) property of θ and φ , i.e., no distinct (i, j) and (i', j') with $\vartheta_{i,j} = \vartheta_{i',j'} > 0$. Let \mathcal{M} denote the set of all valid 1-1 mapping matrices ϑ with $\vartheta_i \in \mathbb{E} \uplus \mathbb{N}$. For any $\vartheta \in \mathcal{M}$, The corresponding I_+ , θ , and φ are recovered as

$$I_+ = \{\ell_i \in I \uplus \mathbb{B}_+ : \vartheta_{i,1} \geq 0\}, \quad \theta(\ell_i) = \vartheta_{i,1}, \quad (31)$$

$$\varphi(\ell_i, \ell_j, m) = \vartheta_{i,j-N_I^o+1+(m-1)N^r}.$$

For $\mathbf{r} \in \mathbb{E} \uplus \mathbb{N}$ and $\ell_i \in I \uplus \mathbb{B}_+$, the association weight is

$$\tilde{w}_i^{(I,\xi)}(\mathbf{r}) = \begin{cases} 1 - \bar{P}_\xi(\ell_i) & \text{if } \mathbf{r} \in \mathbb{N}, \\ \bar{P}_\xi(\ell_i) \eta_{\mathcal{U}}^{(\xi, \mathbf{r})}(\ell_i) & \text{if } \mathbf{r} \in \mathbb{E}, \mathcal{V}_i(\mathbf{r}) = 1, \\ 0 & \text{otherwise,} \end{cases} \quad (32)$$

where $\bar{P}_\xi(\ell_i)$ is the survival probability $\bar{P}_S^{(\xi)}$ for $\ell_i \in I$ or birth probability r_{B+} for $\ell_i \in \mathbb{B}_+$. The indicator $\mathcal{V}_i(\mathbf{r})$ enforces valid associations by preventing self-reflection and duplicate measurement assignments:

$$\mathcal{V}_i(\mathbf{r}) = \begin{cases} 0 & \text{if } \exists i' \neq i, \mathbf{r}^{(i)} = \mathbf{r}^{(i')} > 0; \text{ or if } i > N_I^o, \\ & \exists m \in M, \mathbf{r}^{(i-N_I^o+1+(m-1)N^r)} > 0 \\ 1 & \text{otherwise.} \end{cases}$$

The normalization term is

$$\eta_{\mathcal{U}(Z)}^{(\xi, \mathbf{r})}(\ell_i) = \int \bar{p}_+^{(\xi)}(x, \ell) \hat{\Psi}_{\mathcal{U}(Z)}^{(\mathbf{r})}(x, \ell) dx, \quad (33a)$$

Algorithm 1: Gibbs Sampling

Input: $\vartheta^{(1)}, T, \tilde{w}_i^{(I,\xi)} = [\tilde{w}_i^{(I,\xi)}(\mathbf{r})]_{i=1:N, \mathbf{r} \in \mathbb{E} \uplus \mathbb{N}}$
Output: $\vartheta^{(1)}, \dots, \vartheta^{(T)}$

```

1 for  $t = 2 : T$  do
2   for  $i = 1 : N$  do
3     for  $\mathbf{r} \in \mathbb{E} \uplus \mathbb{N}$  do
4       if any positive entry of  $\mathbf{r}$  is in  $\vartheta_i^{(t)}$  then
5          $\tilde{w}_i^{(I,\xi)}(\mathbf{r}) \leftarrow 0$ ;
6        $\vartheta_i^{(t)} \sim \text{Categorical}(\mathbb{E} \uplus \mathbb{N}, \tilde{w}_i^{(I,\xi)})$ ;
7      $\vartheta^{(t)} \leftarrow [\vartheta_1^{(t)}, \dots, \vartheta_N^{(t)}]$ .

```

$$\hat{\Psi}_{\mathcal{U}(Z)}^{(\mathbf{r})}(\mathbf{x}) = \psi_{D, \mathcal{U}(Z)}^{(\mathbf{r}^{(1)})}(\mathbf{x}) \prod_{j=2, \dots, \dim(\mathbf{r}), m=\lceil (j-1)/N^r \rceil}^N \hat{\psi}_{R, \mathcal{U}(Z)}^{(\mathbf{r}^{(j)}, \ell_{j^*}, m)}(\mathbf{x}), \quad (33b)$$

where $\dim(\cdot)$ denotes vector dimension.

Proposition 3: For any $(I_+, \theta, \varphi) \in \mathcal{F}(\mathbb{L} \uplus \mathbb{B}_+) \times \Theta_{\mathbf{X}, \tilde{\mathbf{T}}}^{\mathcal{U}}$ and its equivalent representation ϑ , the joint component weight is the product of association weights

$$w_{\mathcal{U}}^{(I, I_+, \xi, \theta, \varphi)} = \mathbb{1}_{\mathcal{M}}(\vartheta) \prod_{i=1}^N \tilde{w}_i^{(I, \xi)}(\vartheta_i). \quad (34)$$

Proof: From (31), comparison of (13) and (33b) gives $\hat{\Psi}_{\mathcal{U}}^{(\vartheta_i)} = \hat{\Psi}_{\mathcal{U}}^{(\theta, \varphi)}$ and $\eta_{\mathcal{U}}^{(\xi, \vartheta_i)} = \eta_{\mathcal{U}}^{(\xi, \theta, \varphi)}$. Using (32) yields

$$\prod_{i=1}^{N_I} \tilde{w}_i^{(I, \xi)}(\vartheta_i) = [1 - \bar{P}_S^{(\xi)}]^{I-I_+} [\bar{P}_S^{(\xi)} \eta_{\mathcal{U}}^{(\xi, \theta, \varphi)}]^{I \cap I_+},$$

$$\prod_{i=N_I+1}^N \tilde{w}_i^{(I, \xi)}(\vartheta_i) = [1 - r_{B+}]^{B+ - I_+} [r_{B+} \eta_{\mathcal{U}}^{(\xi, \theta, \varphi)}]^{B+ \cap I_+}.$$

Combining the two expressions recovers (34) from (29), completing the proof.

Proposition 3 shows that selecting high-weight child components (I_+, θ, φ) is equivalent to selecting 1-1 association matrices $\vartheta \in \mathcal{M}$ that maximize the product $\prod_{i=1}^N \tilde{w}_i^{(I, \xi)}(\vartheta_i)$.

B. Gibbs Sampling

Ranked assignment methods such as Murty's algorithm [46] can be employed to extract the T most significant child components of each GLMB component. However, these methods become computationally prohibitive in high-dimensional settings, and the ranked order is unnecessary for the MPET-GLMB filter. Instead, the association mapping ϑ is treated as a realization of a random variable with distribution $\pi(\vartheta) \propto \mathbb{1}_{\mathcal{M}}(\vartheta) \prod_{i=1}^N \tilde{w}_i^{(I, \xi)}(\vartheta_i)$ as proposed in [36]. This formulation assigns nonzero probabilities only to valid mappings and favors mappings with higher weights.

A block Gibbs sampler is used to sample ϑ row by row, with a Markov transition kernel

$$\pi(\vartheta' | \vartheta) = \prod_{n=1}^N \pi_n(\vartheta'_n | \vartheta'_{1:n-1}, \vartheta_{n+1, N})$$

$$= \prod_{n=1}^N \frac{\pi(\vartheta'_{1:n-1}, \vartheta_{n+1:N})}{\sum_{\vartheta_n} \pi(\vartheta'_{1:n-1}, \vartheta_n, \vartheta_{n+1:N})}. \quad (35)$$

For each $n \in \{1, \dots, N\}$, define $\vartheta_{\bar{n}} = (\vartheta_{1:n-1}, \vartheta_{n+1:N})$. Following Proposition 3 in [36] and Proposition 6 in [35], the conditional distribution is

$$\pi_n(\vartheta_n | \vartheta_{\bar{n}}) \propto \begin{cases} \tilde{w}_n^{(I, \xi)}(\vartheta_n) & \text{if no } i \in \vartheta_n, j \in \vartheta_{\bar{n}}, \\ & \text{satisfy } i = j > 0, \\ 0 & \text{otherwise.} \end{cases} \quad (36)$$

The sampling procedure is summarized in Algorithm 1. In terms of computational complexity, Murty's algorithm requires $O(T([S+1]^{3N^r+1} + N^3)$ operations [46], whereas the proposed Gibbs sampler reduces the complexity to $O(TN^2[(S+1)^{3N^r+1} + 1])$, since each row update samples a categorical distribution with cost $O(N[(S+1)^{3N^r+1} + 1])$ [35].

C. MPET-GLMB Filter

1) *Joint Prediction and Update Implementation:* Following [36], prior δ -GLMB density (3) is rewritten as

$$\pi(\mathbf{X}) = \Delta(\mathbf{X}) \sum_{h=1}^H w^{(h)} \delta_{I^{(h)}}(\mathcal{L}(\mathbf{X})) [p^{(h)}]^{\mathbf{X}}, \quad (37)$$

where $w^{(h)} = w^{(I^{(h)}, \xi^{(h)})}$, $p^{(h)} = p^{(\xi^{(h)})}$. The original GLMB parameters $w^{(I, \xi)}$, $p^{(\xi)}$, and $(I, \xi) \in \mathcal{F}(\mathbb{L}) \times \Xi$ are enumerated as $\{(I^{(h)}, \xi^{(h)}, w^{(h)}, p^{(h)})\}_{h=1}^H$. After replacing the component index (I, ξ) by h , the predicted single-target density and survival probability are denoted by

$$\bar{p}_+^{(h)}(x, \ell_i) = \bar{p}_+^{(\xi^{(h)})}(x, \ell_i), \quad \bar{P}_S^{(h)}(\ell_i) = \bar{P}_S^{(\xi^{(h)})}(\ell_i).$$

Since the number of measurement partitions grows combinatorially with the size of the measurement set [29], exhaustive enumeration in (28) is generally intractable. Thus, clustering methods (e.g., distance-based clustering [42] and DBSCAN [47]) are applied to obtain a set of likely partitions, denoted by $\mathcal{P}(Z) = \{\mathcal{U}^{(u)}\}_{u=1}^{|\mathcal{P}(Z)|}$. The association weight in (32) becomes

$$\tilde{w}_i^{(u, h)}(\mathbf{r}) = \begin{cases} 1 - \bar{P}_h(\ell_i) & \text{if } \mathbf{r} \in \mathbb{N}^{(h)}, \\ \bar{P}_h(\ell_i) \eta_Z^{(u, h, \mathbf{r})}(\ell_i) & \text{if } \mathbf{r} \in \mathbb{E}^{(u, h)}, \mathcal{V}_i(\mathbf{r}) = 1, \\ 0 & \text{otherwise,} \end{cases} \quad (38)$$

where $\bar{P}_h(\ell_i)$ is the survival probability $\bar{P}_S^{(h)}$ for $\ell_i \in I$ or birth probability r_{B+} for $\ell_i \in \mathbb{B}_+$, $\eta_Z^{(u, h, \mathbf{r})}(\ell_i) = \eta_{\mathcal{U}^{(u)}}^{(\xi^{(h)}, \mathbf{r})}(\ell_i)$, $\mathbb{N}^{(h)} = \{-1\}^{3|\mathcal{R}(I^{(h)})|+1}$, $\mathbb{E}^{(u, h)} = \{0 : |\mathcal{U}^{(u)}|\}^{3|\mathcal{R}(I^{(h)})|+1}$, with $\mathcal{R}(I)$ denoting the set of reflector labels in I .

Algorithm 2 summarizes the computation of posterior δ -GLMB parameters $\{(I_Z^{(h_z)}, w_Z^{(h_z)}, p_Z^{(h_z)})\}_{h_z=1}^{H_z}$, where $\xi^{(h)}$ is omitted for brevity as it is implicit in h . From (15), (31), and (34), each updated component indexed by (u, h, t) has

$$I_Z^{(u, h, t)} = \{\ell_i \in I^{(h)} \uplus \mathbb{B}_+ : \vartheta_{i,1}^{(u, h, t)} \geq 0\},$$

$$w_Z^{(u, h, t)} \propto w^{(h)} \prod_{i=1}^{|I^{(h)} \uplus \mathbb{B}_+|} \tilde{w}_i^{(u, h)}(\vartheta_i^{(u, h, t)}), \quad (39)$$

$$p_Z^{(u, h, t)}(x, \ell_i) = \bar{p}_+^{(h)}(x, \ell_i) \hat{\Psi}_{\mathcal{U}^{(u)}}^{(\vartheta_i^{(h, t)})}(x, \ell_i) / \eta_Z^{(u, h, \vartheta_i^{(h, t)})}(\ell_i).$$

Algorithm 2: Joint Prediction and Update

Input: $\{(I^{(h)}, w^{(h)}, p^{(h)})\}_{h=1}^H, Z, H_{\max}$

Output: $\{(I_Z^{(h_z)}, w_Z^{(h_z)}, p_Z^{(h_z)})\}_{h_z=1}^{H_z}$

- 1 Sample $[T^{(h)}]_{h=1}^H$ from a multinomial distribution with H_{\max} trials and event probabilities of $[w^{(h)}]_{h=1}^H$;
- 2 Generate partitions $\mathcal{P}(Z) = \{\mathcal{U}^{(u)}\}$ via clustering;
- 3 **for** $u = 1 : |\mathcal{P}(Z)|, h = 1 : H$ **do**
- 4 Initialize $\vartheta^{(u, h, 1)}$;
- 5 Compute weights $\tilde{w}^{(u, h)} = \{\tilde{w}_i^{(u, h)}(\mathbf{r})\}$ using (38);
- 6 $\{\vartheta^{(u, h, t)}\}_{t=1}^{\tilde{T}^{(u, h)}} \leftarrow \text{Unique}(\text{Gibbs}(\vartheta^{(u, h, 1)}, T^{(h)}, \tilde{w}^{(u, h)}))$;
- 7 **for** $t = 1 : \tilde{T}^{(u, h)}$ **do**
- 8 Compute $I_Z^{(u, h, t)}, w_Z^{(u, h, t)}, p_Z^{(u, h, t)}$ using (39);
- 9 $\{(\{I_Z^{(h_z)}, p_Z^{(h_z)}\})_{h_z=1}^{H_z}, [U_{u, h, t}]\} \leftarrow \text{Unique}(\{(\{I_Z^{(u, h, t)}, p_Z^{(u, h, t)}\})_{(u, h, t)=(1, 1, 1)}^{(|\mathcal{P}(Z)|, H, \tilde{T}^{(u, h)})})$;
- 10 **for** $h_z = 1 : H_z$ **do**
- 11 $w_Z^{(h_z)} \leftarrow \sum_{u, h, t: U_{u, h, t}=h_z} w_Z^{(u, h, t)}$;
- 12 Normalize weights $\{w_Z^{(h_z)}\}_{h_z=1}^{H_z}$.

Duplicated GLMB components are merged by summing their weights, after which the remaining weights are normalized to obtain the posterior density.

2) *Measurement Driven Adaptive Birth Model:* Existing multipath RFS-based trackers [22], [27], [45] rely on hand-crafted target birth density and fixed multipath propagation models, which limit their applicability in real-world traffic environments. In contrast, the proposed MPET-GLMB filter jointly estimates object and reflector states, enabling online refinement of the multipath model. Moreover, a measurement-driven birth model is incorporated to enhance adaptability in dynamic scenarios. At each scan, the measurement set is partitioned into stationary and moving subsets, $Z = Z_s \uplus Z_m$, where the stationary measurements Z_s satisfy a Doppler threshold $|\dot{r}| < \dot{r}_{\min}$. All measurements are transformed into Cartesian coordinates, denoted by $Z^C = Z_s^C \uplus Z_m^C$. Hough transform [48] is then applied to Z_s^C to detect lines. Stationary measurements within distance d_{\max} of any detected line are retained as potential reflector measurements Z_r^C . Finally, $Z_r^C \uplus Z_m^C$ is clustered to generate feasible measurement partitions.

After computing the posterior δ -GLMB density, newborn targets are generated adaptively from measurements rather than predefined birth models. Each measurement subset in every feasible partition is assigned a unique new label, forming the birth label set \mathbb{B}_+ that satisfies $\mathbb{B}_+ \cap \mathbb{L} = \emptyset$. For $W_B \subseteq Z_r \uplus Z_m$, the associated birth label is denoted ℓ_{W_B} . The likelihood that W_B initializes a new target is defined as

$$\tilde{r}_B(\ell_{W_B}) = 1 - \frac{\sum_{u, h, t} \mathbb{1}_{\mathcal{U}_Z^{(u, h, t)}}(W_B) w_Z^{(u, h, t)}}{\sum_{u, h, t} w_Z^{(u, h, t)}},$$

¹{.} represents a MATLAB cell data structure which may contain duplicated elements; Unique(.) returns the unique elements of a cell, and also the indices of these elements in the original cell if required.

where $\mathcal{U}_Z^{(u,h,t)}$ denotes the measurement subset associated with $\vartheta^{(u,h,t)}$, and $1_{\mathcal{U}_Z^{(u,h,t)}}(W_B)$ indicates whether W_B is assigned to an existing target [34], [49]. If W_B is used in all hypotheses, then $\tilde{r}_B(W_B) = 0$, meaning no new target can be initialized. The resulting birth density (7) has existence probabilities

$$r_{B+}(\ell_{W_B}) = \begin{cases} r_{B_{\max}} \tilde{r}_B(\ell_{W_B}) & \text{if } \tilde{r}_B(\ell_{W_B}) > r_{B_{\min}}, \\ 0 & \text{if } \tilde{r}_B(\ell_{W_B}) \leq r_{B_{\min}}, \end{cases}$$

where $r_{B_{\max}} \in [0, 1]$ is the maximum existence probability, and $r_{B_{\min}}$ is the initialize threshold.

The spatial extent of a newborn target initialized from W_B is estimated from the measurement distribution. Let \bar{W}_B^C and C_{W_B} denote the mean and covariance of the measurement locations in Cartesian coordinates, respectively. Following the Gaussian approximation of elliptical extents [7], the extent matrix is estimated as C_{W_B}/ϱ . Eigenvalue decomposition of the extent yields the heading vector u_{W_B} associated with the largest eigenvalue d_{W_B} .

If W_B is stationary and aligned with a detected line, a newborn reflector is initialized using a particle set $\mathcal{X}_{W_B} = \{(x_{K,W_B}^{(l)}, x_{E,W_B}^{(l)}, \lambda_{W_B}^{(l)})\}_{l=1}^L$, where

$$\begin{aligned} \lambda_{W_B}^{(l)} &= 1/L, \quad x_{K,W_B}^{(l)} \sim \mathcal{N}(\bar{W}_B^C, G_+ Q_+ G_+^T), \\ x_{E,W_B}^{(l)} &\sim \mathcal{N}([\angle(u_{W_B}), -d_{W_B}/2, d_{W_B}/2]^T, Q_{E+}). \end{aligned}$$

Otherwise, a new object is initialized with a GGIW density

$$\begin{aligned} p_{B+}(x, \ell_{W_B}) &= \mathcal{GGIW}(x; \chi_{W_B}) = \mathcal{G}(x_\gamma; \alpha_{W_B}, \beta_{W_B}) \\ &\times \mathcal{N}(x_K; \mu_{W_B}, P_B) \mathcal{IW}(x_E; \nu_B, V_{W_B}), \end{aligned}$$

where the kinematic covariance P_B and inverse Wishart degrees of freedom ν_B are predefined, and

$$\begin{aligned} \alpha_{W_B} &= |W_B|^2/\gamma_{\text{var}}, \quad \beta_{W_B} = |W_B|/\gamma_{\text{var}}, \\ \mu_{W_B} &= \bar{W}_B^C, \quad V_{W_B} = C_{W_B}/[\varrho(\nu_B + 3)], \end{aligned}$$

with γ_{var} denoting the measurement rate variance.

3) *Track Extraction and Pruning*: After each joint prediction and update step, labeled target estimates are extracted from the posterior δ -GLMB density. The cardinality is first estimated using the *maximum a posteriori* criterion, and the highest-weight GLMB component with this cardinality is selected, denoted by $(I_Z^{(h_{\max})}, p_Z^{(h_{\max})})$. For each target labeled by $\ell \in I_Z^{(h_{\max})}$, its kinematic and extent states are estimated from the distribution $p_Z^{(h_{\max})}(\cdot, \ell)$. To suppress unlikely hypotheses, the posterior δ -GLMB is pruned by discarding all components with weights below the threshold $w_Z^{(h)} < w_{\min}$. Further implementation details can be found in [29], [31].

V. EXPERIMENTS AND PERFORMANCE ANALYSIS

This section evaluates the performance of the proposed MPET-GLMB filter in two simulated traffic scenarios and one real-world scenario. The method is benchmarked against the state-of-the-art RFS-based multipath multiple extended target tracker (MP-ET-PHD) [27] and a conventional GLMB filter. Since the GLMB and MP-ET-PHD filters rely on fixed object-birth models, they are initialized with newborn components near the true object-birth positions. For ablation studies, a

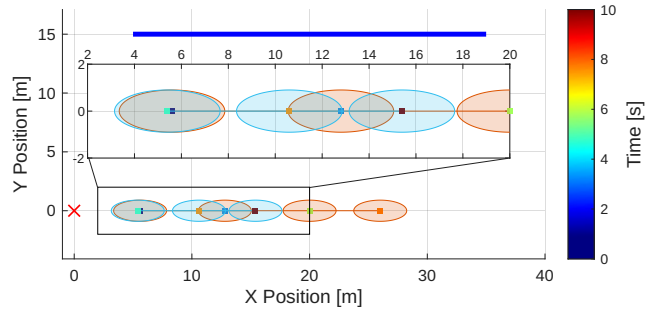


Fig. 2. Simulated ground truth for Scenario 1. The red cross denotes the radar position. The blue thick line represents the reflector. Square markers show the object centroids at selected time steps, with ellipsoids denoting the object spatial extents. Objects are assigned different colors for identification.

TABLE I
TRACKING PERFORMANCE METRICS (SCENARIO 1)

Method	OSPA	OSPA ⁽²⁾	MOTA	MOTP	TP	FP	FN	IDS
MPET-GLMB	0.2291	0.3437	0.9444	0.1677	5777	11	323	5
MPET-GLMB-FB	0.2657	0.5519	0.8844	0.2427	5922	42	178	484
GLMB	0.4814	0.7418	0.6307	0.2371	4817	500	1283	470
MP-ET-PHD	0.2588	/	/	0.2191	5855	11	245	/

* TP, FP, FN, and IDS are cumulative sums over 100 Monte Carlo runs. Other metrics are average values. OSPA, OSPA⁽²⁾, and MOTP are measured in meters. **Bold** denotes the best result.

variant of MPET-GLMB using the same fixed birth model is also evaluated, which is referred to as MPET-GLMB-FB. All filters use the GGIW extended object model in Section III and share identical parameters unless otherwise specified.

Multi-target state estimation accuracy is evaluated using the optimal sub-pattern assignment (OSPA) distance [50], which captures both localization and cardinality errors between the estimated state set \hat{X} and the ground-truth set X . Since OSPA is designed for unlabeled sets and does not account for target identities, the OSPA⁽²⁾ distance is additionally employed to evaluate trajectory-level errors [50]. Moreover, the widely used CLEAR MOT metrics [51], [52], including multi-object tracking accuracy (MOTA), multi-object tracking precision (MOTP), true positives (TP), false positives (FP), false negatives (FN), and ID switches (IDS), are reported in the following evaluation. For the OSPA and OSPA⁽²⁾, the cutoff distance is set to 2 m with an order of 1, and OSPA⁽²⁾ window length is set to 5. For CLEAR MOT evaluation, a distance threshold of 1 m is used to determine true positive matches.

A. Scenario 1

Scenario 1 simulates an occlusion event between objects to evaluate the filter's ability to exploit multipath measurements for robust tracking. As shown in Fig. 2, a stationary reflector of length 30 m is positioned at [20 m, 15 m]^T. Two objects with dimensions 4.5 m × 1.8 m move away from the radar under a constant velocity model. The initial kinematic states are [5 m, 0 m, 3 m/s, 0 m/s]^T and [5 m, 0 m, 2 m/s, 0 m/s]^T, respectively. The first object enters the observation area at 1 s and exits at 8 s. The second object enters at 5 s and remains until the simulation ends at 10 s. When the second object appears, the first object becomes occluded, causing its

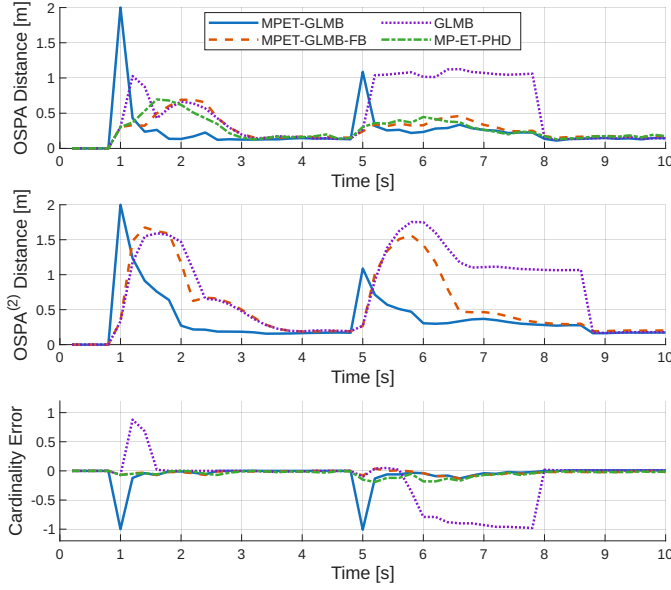


Fig. 3. OSPA distance, OSPA⁽²⁾ distance and cardinality estimation error averaged over 100 Monte Carlo runs for Scenario 1.

detection probabilities via the direct and type 1 two-bounce paths to drop by 90%.

The radar operates at a scan rate of 5 Hz with measurement noise standard deviations $\sigma_r = 0.2$ m, $\sigma_\phi = 0.5^\circ$, and $\sigma_r = 0.5$ m/s. Clutter is uniformly distributed over $(r, \phi) \in [0, 60] \times [-90^\circ, 90^\circ]$ with a Poisson rate of $\gamma_c = 20$. For unoccluded objects, the direct path detection probability is $P_d = 0.95$, while the multi-bounce path detection probability is $P_{d,R} = 0.9$. The measurement rates x_γ of the reflector and two objects are set to 80, 30, and 30, respectively, with a Poisson rate scaling factor of $\gamma_{m \in \{1,2,3\}} = 0.6$.

The birth parameters of the MPET-GLMB filter are configured as $r_{B_{\max}} = 1$, $r_{B_{\min}} = 0.5$, $\gamma_{\text{var}} = 25$, $\nu_B = 10$, and $P_B = \text{diag}(1, 1, 4, 4, 0.03)$. In contrast, the other three filters use a single newborn component with an existence probability of 0.02. Its GGIW parameters are $\chi_B = (\alpha_B, \beta_B, \mu_B, P_B, \nu_B, V_B)$, where $\alpha_B = \bar{x}_\gamma^2 / \gamma_{\text{var}}$, $\beta_B = \bar{x}_\gamma / \gamma_{\text{var}}$, $\mu_B = [4, 0, 0, 0]^T$, $V_B = 4\bar{E}/(\nu_B + 3)$. Here, $\bar{x}_\gamma = 40$ and $\bar{E} = \text{diag}(4, 2)$ are the expected measurement rate and extent matrix for the object, respectively. The object survival probability is set to $P_S = 0.99$. The MP-ET-PHD filter is provided with accurate prior environmental knowledge by setting its multipath measurement model with the exact reflector position and shape. All filters employ the same measurement clustering procedure, and unused stationary measurements are removed for the GLMB and MP-ET-PHD filters.

Tracking performance is evaluated over 100 Monte Carlo runs. As shown in Table I and Fig. 3, MPET-GLMB achieves the highest overall tracking performance among all methods. Although the measurement-driven adaptive birth model requires at least one frame before initializing a new track, causing transient cardinality estimation errors and OSPA peaks when newborn objects appear at 1s and 5s, MPET-GLMB quickly converges to accurate and stable track estimations. Consequently, it attains the lowest average OSPA and OSPA⁽²⁾

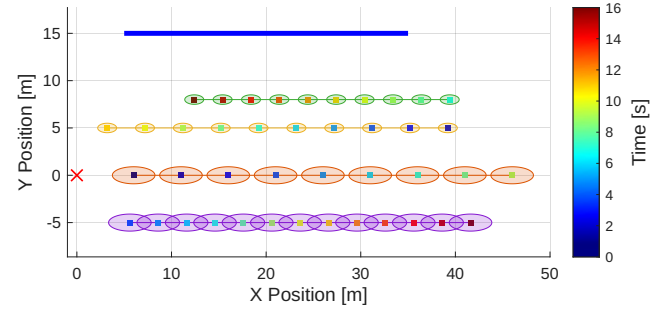


Fig. 4. Simulated ground truth for Scenario 2. The two larger objects in the lower region move from left to right, while the two smaller objects in the upper region move from right to left.

TABLE II
OBJECT SIMULATION PARAMETERS (SCENARIO 2)

ID	Initial State	Dimensions	x_γ	Birth	Death
1	$[5 \text{ m}, 0 \text{ m}, 5 \text{ m/s}, 0 \text{ m/s}]^T$	$4.5 \text{ m} \times 1.8 \text{ m}$	30	1s	9s
2	$[5 \text{ m}, -5 \text{ m}, 3 \text{ m/s}, 0 \text{ m/s}]^T$	$4.5 \text{ m} \times 1.8 \text{ m}$	30	4s	16s
3	$[40 \text{ m}, 5 \text{ m}, -4 \text{ m/s}, 0 \text{ m/s}]^T$	$2 \text{ m} \times 1 \text{ m}$	20	2s	11s
4	$[40 \text{ m}, 8 \text{ m}, -3 \text{ m/s}, 0 \text{ m/s}]^T$	$2 \text{ m} \times 1 \text{ m}$	20	7s	16s

distances and fewest ID-switch errors. In contrast, the MPET-GLMB-FB and MP-ET-PHD filters achieve more accurate cardinality estimation, but their fixed birth components compete with existing tracking hypotheses, resulting in significantly higher ID-switch rates. The GLMB filter performs worst due to the absence of a multipath measurement model, leading to the highest cardinality error and OSPA distances. Specifically, GLMB fails to maintain the track of the first object following its occlusion, whereas the other three filters utilize multipath measurements to obtain reliable estimations. Finally, although MP-ET-PHD achieves OSPA and MOTP performance comparable to MPET-GLMB-FB, it does not estimate target IDs or trajectories. Consequently, the OSPA⁽²⁾, MOTA, and IDS metrics relying on object IDs are not reported for this filter.

B. Scenario 2

Scenario 2 considers a more complex environment in which four objects of distinct shapes enter the observation area from different positions, as detailed in Fig. 4 and Table II. As illustrated in Fig. 5, the type-1 two-bounce multipath measurements overlap with the direct path measurements, posing significant challenges to the filters. Object occlusion is not simulated in this scenario. The fixed birth model comprises four components, each initialized at the true object birth location with an existence probability of 0.01. For the two smaller objects, the expected extent matrix and measurement rate are set to $\bar{E} = \text{diag}(2, 1)$ and $\bar{x}_\gamma = 30$, respectively. All other parameters are identical to those used in Scenario 1.

As shown in Table III and Fig. 6, the proposed MPET-GLMB filter achieves superior tracking performance across all metrics in this challenging scenario. Despite incorporating multipath measurement models, MPET-GLMB-FB and MP-ET-PHD exhibit large cardinality errors, underscoring the effectiveness of the proposed adaptive birth model in complex multipath environments. GLMB and MPET-GLMB-FB tend to

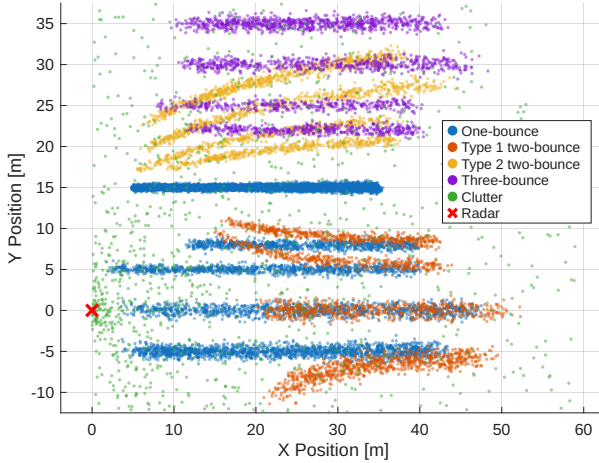


Fig. 5. All measurements in one Monte Carlo run for Scenario 2.

TABLE III
TRACKING PERFORMANCE METRICS (SCENARIO 2)

Method	OSPA	OSPA ⁽²⁾	MOTA	MOTP	TP	FP	FN	IDS
MPET-GLMB	0.2505	0.3804	0.8920	0.1632	18194	872	1206	17
MPET-GLMB-FB	0.3885	0.6122	0.6956	0.1913	17540	3511	1860	534
GLMB	0.6908	0.8686	0.3995	0.1943	17391	9129	2009	512
MP-ET-PHD	0.4664	/	/	0.1826	15541	1145	3859	/

* TP, FP, FN, and IDS are cumulative sums over 100 Monte Carlo runs. Other metrics are average values. OSPA, OSPA⁽²⁾, and MOTP are measured in meters. **Bold** denotes the best result.

overestimate cardinality because type-1 two-bounce measurements repeatedly trigger births near fixed birth components. However, MPET-GLMB-FB mitigates false tracks using its multipath model, resulting in lower OSPA and cardinality errors than GLMB. In comparison, the MP-ET-PHD filter underestimates cardinality due to the Poisson assumptions and inherent limitations of PHD-based approximation of the multi-target density [28]. The consistently low OSPA, MOTP, and IDS demonstrate that MPET-GLMB maintains stable and accurate trajectory estimates.

C. Scenario 3

Radar measurements for Scenario 3 are sourced from the Radar Ghost dataset [53], which focuses on automotive radar ghost targets and provides detailed annotations of multipath measurements, as illustrated in Fig. 7. The selected sequence² contains three pedestrians and one cyclist moving between an automotive radar and a reflective wall. The radar scan rate is 10 Hz, and the mean Cartesian position of each object's one-bounce measurements is used as the ground truth at each scan.

To accommodate the higher variability of real-world radar measurements, the measurement rate variance is increased to $\gamma_{\text{var}} = 64$, and the inverse Wishart degrees of freedom are reduced to $\nu_B = 4$. The fixed birth model comprises four components, each with an existence probability of 0.01, and is initialized at the true birth positions. The expected extent matrix and measurement rate are set to $\bar{E} = \text{diag}(0.5, 0.5)$

²File name: scenario-13_sequences-01-05-05-06_start-frames-013-123-166-019_cycl-ped-ped-ped_train.h5

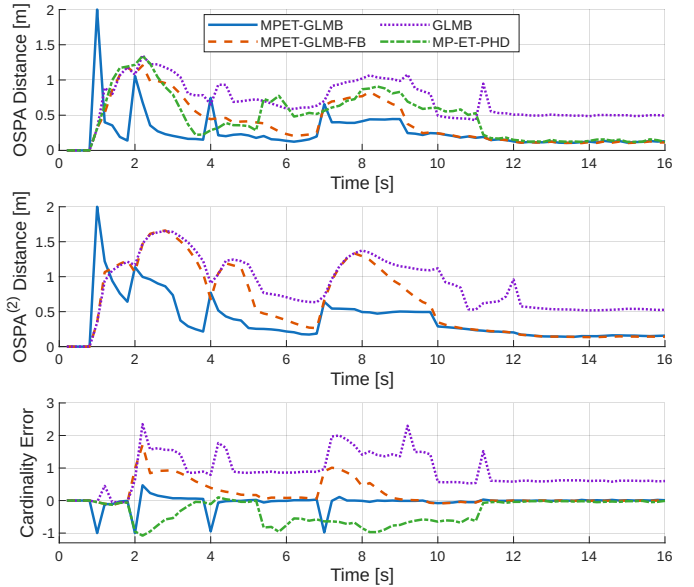


Fig. 6. OSPA distance, OSPA⁽²⁾ distance, and cardinality estimation error averaged over 100 Monte Carlo runs for Scenario 2.

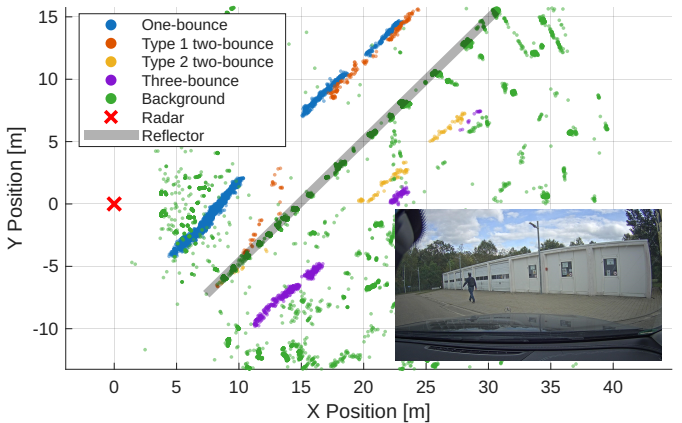


Fig. 7. All radar measurements for Scenario 3. The experimental environment is shown in the lower right corner of the image.

and $\bar{x}_\gamma = 20$, respectively. Since all objects appear at the beginning of the sequence, birth events are restricted to the first three frames for all filters to reduce ID-switch errors. The multipath detection probability is set to $P_{d,R} = 0.8$, while all other parameters follow those in Scenarios 1 and 2.

As shown in Fig. 8 and Table IV, MPET-GLMB outperforms the other filters in both estimation accuracy and track ID consistency within this real-world scenario. Despite restricting births to the first three frames, filters with fixed birth models still exhibit cardinality overestimation and ID switches during the initialization, further demonstrating the advantage of the proposed adaptive birth model. Furthermore, while the three GLMB-based filters maintain accurate cardinality after the initial period, the MP-ET-PHD consistently underestimates the number of objects after 1.5 s, which may pose safety concerns in real-world traffic applications.

TABLE IV
TRACKING PERFORMANCE METRICS (SCENARIO 3)

Method	OSPA	OSPA ⁽²⁾	MOTA	MOTP	TP	FP	FN	IDS
MPET-GLMB	0.2147	0.3076	0.9375	0.0957	105	0	7	0
MPET-GLMB-FB	0.2153	0.4218	0.8482	0.1011	109	7	3	7
GLMB	0.2273	0.5140	0.8214	0.1045	110	10	2	8
MP-ET-PHD	0.4301	/	/	0.1093	93	0	19	/

* OSPA, OSPA⁽²⁾, and MOTP are measured in meters. **Bold** denotes the best result.

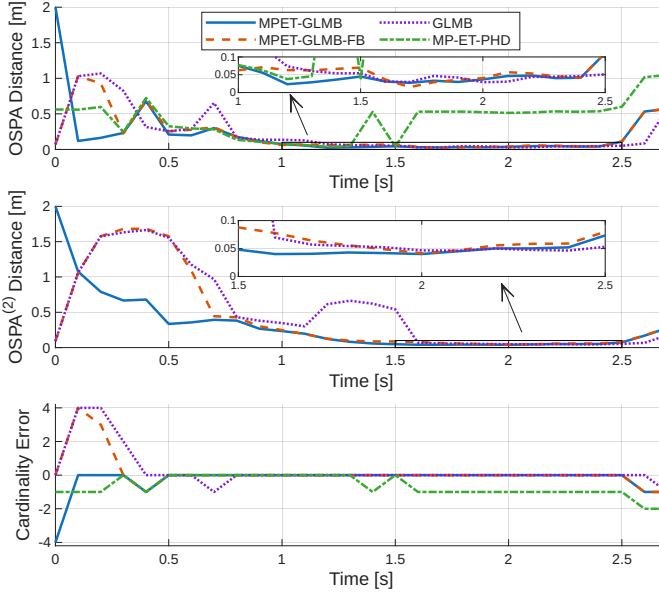


Fig. 8. OSPA distance, OSPA⁽²⁾ distance, and cardinality estimation error for Scenario 3.

D. Ablation Study

To assess the individual contributions of the uniform stick reflector model, Gibbs sampling-based truncation, and the adaptive birth model, ablation experiments are conducted in Scenario 2 with variants of the MPET-GLMB filter. As summarized in Table V, MPET-GLMB-FB replaces the adaptive birth model with a fixed birth model (detailed in Section V-B), MPET-GLMB-GGIW replaces the uniform stick reflector model with a standard GGIW model, and MPET-GLMB-MA replaces the Gibbs sampling with Murty's algorithm.

Reflector extent estimation accuracy is evaluated using the Hausdorff distance. Given a reflector extent state x_E , let $\mathcal{C} = \{C_{\text{start}}, C_{\text{end}}\}$ denote the endpoints computed via (18). For MPET-GLMB-GGIW, the reflector heading and length are extracted from the eigenvalue decomposition of x_E . The Hausdorff distance is given by

$$d_H(\hat{\mathcal{C}}, \mathcal{C}) = \max \left[\max_{\hat{C} \in \hat{\mathcal{C}}} d_{\mathcal{C}}(\hat{C}), \max_{C \in \mathcal{C}} d_{\hat{\mathcal{C}}}(C) \right],$$

where $d_{\mathcal{C}}(\hat{C})$ denotes the minimum distance from an estimated endpoint \hat{C} to the ground truth line segment. Computational efficiency is assessed using the average frames processed per second (FPS) on the same simulation platform.

As shown in Table V, MPET-GLMB-MA achieves the highest tracking accuracy, slightly surpassing the proposed MPET-GLMB, as Murty's algorithm guarantees optimal assignments.

TABLE V
TRACKING PERFORMANCE METRICS (ABLATION STUDY)

Method	OSPA \downarrow	OSPA ⁽²⁾ \downarrow	MOTA \uparrow	IDS \downarrow	$d_H\downarrow$	FPS \uparrow
MPET-GLMB	0.2505	0.3804	0.8920	17	2.17	3.51
MPET-GLMB-FB	0.3885	0.6122	0.6956	534	2.20	2.21
MPET-GLMB-GGIW	0.2972	0.4831	0.8153	187	11.32	4.87
MPET-GLMB-MA	0.2466	0.3792	0.8969	16	2.13	0.089

* IDS is a cumulative sum over 100 Monte Carlo runs. Other metrics are average values. OSPA, OSPA⁽²⁾, and d_H are measured in meters.

However, its high computational cost substantially reduces the FPS, whereas the Gibbs sampling-based implementation provides an approximately 40 times speedup. Consistent with the analysis in Section V-B, MPET-GLMB-FB exhibits degraded accuracy due to the fixed birth model, with additional false tracks further reducing efficiency. Regarding reflector modeling, MPET-GLMB-GGIW produces significantly larger Hausdorff distances, indicating that the GGIW model inadequately captures the linear geometry of reflectors. These extent estimation errors also lead to increased ID switches. Although MPET-GLMB-GGIW achieves slightly higher FPS due to lower computational cost, the resulting accuracy loss is substantial. Overall, the ablation results confirm that each proposed module contributes as intended, and MPET-GLMB achieves an effective balance between tracking accuracy and real-time efficiency.

VI. CONCLUSION

This paper presented the multipath extended target generalized labeled multi-Bernoulli (MPET-GLMB) filter, a unified Bayesian framework for tracking multiple extended targets in dynamic multipath environments. By integrating the labeled RFS formulation with extended target modeling, the proposed method jointly resolves the uncertainties in target existence, measurement partitioning, and measurement-to-path association. A Gibbs sampling-based joint prediction and update strategy was developed to maintain computational tractability, together with a measurement-driven adaptive birth model to enable robust track initialization. Extensive experiments on simulated traffic scenarios and real-world automotive radar data demonstrated that the MPET-GLMB filter consistently outperforms state-of-the-art methods in state estimation accuracy and trajectory continuity, particularly under severe occlusion and dense target birth conditions. Future work will investigate extensions to multi-sensor fusion and real-time deployment on embedded hardware platforms.

APPENDIX A GGIW PARAMETERS UPDATE

Given the prior GGIW density $p(x) = \mathcal{GGIW}(x; \chi)$ and the associated measurement subset W , the posterior density is $p(x|W) = \frac{\tilde{p}(x|W)}{\int \tilde{p}(x|W) dx}$, where the unnormalized density is

$$\begin{aligned} \tilde{p}(x|W) &= \mathcal{G}(\chi; \alpha, \beta) \mathcal{N}(x_K; \mu, P) \mathcal{IW}(x_E; \nu, V) \\ &\quad \times \mathcal{PS}(|W|; \gamma_m x_\gamma) \prod_{z \in W} \mathcal{N}(z; \hat{h}_m(x_K), R_m(x_E)). \end{aligned}$$

The product of gamma and Poisson PDFs can be written as

$$\begin{aligned} \mathcal{G}(x_\gamma; \alpha, \beta) \mathcal{PS}(|W|; \gamma_m x_\gamma) \\ = \frac{\beta^\alpha}{\Gamma(\alpha)} x_\gamma^{\alpha-1} e^{-\beta x_\gamma} \frac{(\gamma_m x_\gamma)^{|W|} e^{-\gamma_m x_\gamma}}{|W|!} \\ = \mathcal{G}(x_\gamma; \alpha_W, \beta_W) \eta_\gamma, \end{aligned}$$

where $\eta_\gamma = \frac{\beta^\alpha \Gamma(\alpha+|W|) \gamma_m^{|W|}}{\Gamma(\alpha)(\beta+\gamma_m)^{(\alpha+|W|)} |W|!}$, $\alpha_W = \alpha + |W|$, and $\beta_W = \beta + \gamma_m$. Since x_γ is independent of x_K and x_E , the posterior density of the measurement rate becomes

$$p(x_\gamma | W) = \frac{\eta_\gamma \mathcal{G}(x_\gamma; \alpha_W, \beta_W)}{\int \eta_\gamma \mathcal{G}(x_\gamma; \alpha_W, \beta_W) dx_\gamma} = \mathcal{G}(x_\gamma; \alpha_W, \beta_W).$$

It remains to compute $\tilde{p}(x_K, x_E | W) = \mathcal{N}(x_K; \mu, P) \times \mathcal{IW}(x_E; \nu, V) \eta_N(W, R_m) \prod_{z \in W} \mathcal{N}(z; \hat{h}_m(x_K), R_m)$ and its integral $\int \tilde{p}(x_K, x_E | W) dx$.

Following [42, Appendix A], the product of Gaussian PDFs over $z \in W$ can be written as

$$\prod_{z \in W} \mathcal{N}(z; \hat{h}_m(x_K), R_m) = \eta_N(W, R_m) \mathcal{N}(\bar{z}; \hat{h}_m(x_K), \frac{R_m}{|W|}),$$

where $\eta_N(W, R_m) = (2\pi)^{\frac{3(1-|W|)}{2}} |R_m|^{\frac{1-|W|}{2}} e^{\text{tr}(-\frac{1}{2} D R_m^{-1})}$ and $D = \sum_{z \in W} (z - \bar{z})(z - \bar{z})^T$. The EKF linearization yields $\mathcal{N}(x_K; \mu, P) \mathcal{N}(\bar{z}; \hat{h}_m(x_K), \frac{R_m}{|W|}) \approx \mathcal{N}(x_K; \mu_W, P_W) \times \mathcal{N}(\bar{z}; \hat{h}_m(\mu), \Lambda)$, where

$$\begin{aligned} \mu_W &= \mu + K(\bar{z} - \hat{h}_m(\mu)), \quad P_W = P - K \Lambda K^T, \\ K &= P H_m^T \Lambda^{-1}, \quad \Lambda = H_m P H_m^T + R_m(\bar{E})/|W|. \end{aligned} \quad (40)$$

Notably, the EKF innovation covariance $\bar{\Lambda} = H_m P H_m^T + R_m(x_E)/|W|$ originally depends on x_E . Since $R_m(x_E)$ has minor effects on $\bar{\Lambda}$ when $|W|$ is large, we approximate it by substituting x_E with the expectation $\bar{E} = V/(\nu - 3)$ in (40).

As x_E is symmetric positive-definite, the matrix determinant lemma yields the approximation:

$$\begin{aligned} |R_m| &= \sigma_r^2 |\varrho \check{H}_m x_E \check{H}_m^T + \text{diag}(\sigma_r^2, \sigma_\phi^2)| \\ &= \sigma_r^2 \sigma_\phi^2 |x_E^{-1} + \varrho \check{H}_m^T \text{diag}(\sigma_r^{-2}, \sigma_\phi^{-2}) \check{H}_m| |x_E| \\ &\approx \sigma_r^2 \sigma_\phi^2 |\bar{E}^{-1} + \varrho \check{H}_m^T \text{diag}(\sigma_r^{-2}, \sigma_\phi^{-2}) \check{H}_m| |x_E| \\ &= \eta_R |x_E|. \end{aligned} \quad (41)$$

We approximate R_m^{-1} using the first-order Neumann series

$$\begin{aligned} R_m^{-1} &= \text{diag} \left([\varrho \check{H}_m x_E \check{H}_m^T + \text{diag}(\sigma_r^2, \sigma_\phi^2)]^{-1}, \sigma_r^{-2} \right) \quad (42) \\ &\approx \text{diag} \left((\varrho \check{H}_m x_E \check{H}_m^T)^{-1} - \check{E}^{-1} \text{diag}(\sigma_r^2, \sigma_\phi^2) \check{E}^{-1}, \sigma_r^{-2} \right), \end{aligned}$$

where $\check{E} = \varrho \check{H}_m \bar{E} \check{H}_m^T$. Furthermore, we have

$$\begin{aligned} \eta_N(W, R_m) \mathcal{IW}(x_E; \nu, V) \\ = (2\pi)^{\frac{3(1-|W|)}{2}} |R_m|^{\frac{1-|W|}{2}} |V|^{\frac{\nu}{2}} |x_E|^{\frac{-(\nu+3)}{2}} e^{\frac{-\text{tr}(D R_m^{-1} + V x_E^{-1})}{2}} \\ \approx (2\pi)^{\frac{3(1-|W|)}{2}} \eta_R^{\frac{1-|W|}{2}} |V|^{\frac{\nu}{2}} |x_E|^{\frac{-(\nu+|W|+2)}{2}} e^{\frac{\text{tr}(D \Omega)}{2}} \\ \times e^{\frac{-\text{tr}[(V + \check{H}_m^{-1} \check{D}(\check{H}_m^{-1})^T / \varrho) x_E^{-1}]}{2}} \\ = \eta_R^{\frac{1-|W|}{2}} \eta_{\mathcal{IW}} \mathcal{IW}(x_E; \nu_W, V_W), \end{aligned} \quad (43)$$

where \check{D} is the upper-left 2×2 submatrix of D , $\Omega = \text{diag}(\check{E}^{-1} \text{diag}(\sigma_r^2, \sigma_\phi^2) \check{E}^{-1}, -\sigma_r^{-2})$, $\nu_W = \nu + |W| - 1$, and $V_W = V + \check{H}_m^{-1} \check{D}(\check{H}_m^{-1})^T / \varrho$. The approximation in the second line of (43) follows from (41) and (42), with $\text{tr}(D R_m^{-1})$ evaluated using the properties of matrix trace:

$$\begin{aligned} \text{tr}[D \text{diag}((\varrho \check{H}_m x_E \check{H}_m^T)^{-1} - \check{E}^{-1} \text{diag}(\sigma_r^2, \sigma_\phi^2) \check{E}^{-1}, \sigma_r^{-2})] \\ = \text{tr}[(\check{H}_m^{-1} \check{D}(\check{H}_m^{-1})^T / \varrho) x_E^{-1}] - \text{tr}(D \Omega). \end{aligned}$$

Consequently, $\mathcal{GGIW}(x | \chi_W)$ is the approximated posterior density, and the marginal likelihood is $\int \tilde{p}(x | W) \approx \eta_\gamma \mathcal{N}(\bar{z}; \hat{h}_m(\mu), \Lambda) \eta_R^{(1-|W|)/2} \eta_{\mathcal{IW}}$.

REFERENCES

- [1] Y. Bar-Shalom, P. K. Willett, and X. Tian, *Tracking and data fusion*. Storrs, CT, USA: YBS publishing, 2011.
- [2] T. Fortmann, Y. Bar-Shalom, and M. Scheffe, “Sonar tracking of multiple targets using joint probabilistic data association,” *IEEE J. Ocean. Eng.*, vol. 8, no. 3, pp. 173–184, Jul. 1983.
- [3] D. Reid, “An algorithm for tracking multiple targets,” *IEEE Trans. Autom. Control*, vol. 24, no. 6, pp. 843–854, Dec. 1979.
- [4] F. Papi, B.-N. Vo, B.-T. Vo, C. Fantacci, and M. Beard, “Generalized labeled multi-Bernoulli approximation of multi-object densities,” *IEEE Trans. Signal Process.*, vol. 63, no. 20, pp. 5487–5497, Oct. 2015.
- [5] J. Liu, L. Bai, Y. Xia, T. Huang, B. Zhu, and Q.-L. Han, “GNN-PMB: A simple but effective online 3D multi-object tracker without bells and whistles,” *IEEE Trans. Intell. Veh.*, vol. 8, no. 2, pp. 176–1189, Feb. 2023.
- [6] G. Ding *et al.*, “OptiPMB: Enhancing 3D multi-object tracking with optimized Poisson multi-Bernoulli filtering,” *IEEE Trans. Intell. Transp. Syst.*, vol. 26, no. 12, pp. 22312–22328, Oct. 2025.
- [7] M. Feldmann, D. Fränken, and W. Koch, “Tracking of extended objects and group targets using random matrices,” *IEEE Trans. Signal Process.*, vol. 59, no. 4, pp. 1409–1420, Apr. 2011.
- [8] F. Meyer and J. Williams, “Scalable detection and tracking of geometric extended objects,” *IEEE Trans. Signal Process.*, vol. 69, pp. 6283–6298, Oct. 2021.
- [9] Y. Xia, Á. F. García-Fernández, F. Meyer, J. L. Williams, K. Granström, and L. Svensson, “Trajectory PMB filters for extended object tracking using belief propagation,” *IEEE Trans. Aerosp. Electron. Syst.*, vol. 59, no. 6, pp. 9312–9331, Dec. 2023.
- [10] J. Liu *et al.*, “Which framework is suitable for online 3D multi-object tracking for autonomous driving with automotive 4D imaging radar?” in *Proc. IEEE Intell. Vehicles Symp. (IV)*, 2024, pp. 1258–1265.
- [11] M. Baum and U. D. Hanebeck, “Random hypersurface models for extended object tracking,” in *Proc. IEEE Int. Symp. Signal Process. Inf. Technol. (ISSPIT)*, 2009, pp. 178–183.
- [12] M. Baerveldt, M. E. López, and E. F. Brekke, “Extended target PMBM tracker with a Gaussian process target model on LiDAR data,” in *Proc. 26th Int. Conf. Inf. Fusion (FUSION)*, 2023, pp. 1–8.
- [13] G. Ding, J. Liu, Y. Xia, T. Huang, B. Zhu, and J. Sun, “LiDAR point cloud-based multiple vehicle tracking with probabilistic measurement-region association,” in *Proc. 27th 15th Int. Conf. Inf. Fusion (FUSION)*, 2024, pp. 1–8.
- [14] T. Visentin, J. Hasch, and T. Zwick, “Analysis of multipath and DOA detection using a fully polarimetric automotive radar,” in *Proc. Eur. Radar Conf. (EURAD)*, 2017, pp. 45–48.
- [15] L. Zheng, J. Long, M. Lops, F. Liu, X. Hu, and C. Zhao, “Detection of ghost targets for automotive radar in the presence of multipath,” *IEEE Trans. Signal Process.*, vol. 72, pp. 2204–2220, Apr. 2024.
- [16] R. Prophet, J. Martinez, J.-C. F. Michel, R. Ebelt, I. Weber, and M. Vossiek, “Instantaneous ghost detection identification in automotive scenarios,” in *Proc. IEEE Radar Conf. (RadarConf)*, 2019, pp. 1–6.
- [17] M. Chamseddine, J. Rambach, D. Stricker, and O. Wasenmuller, “Ghost target detection in 3D radar data using point cloud based deep neural network,” in *Proc. 25th Int. Conf. Pattern Recognit. (ICPR)*, 2021, pp. 10398–10403.
- [18] N. Scheiner *et al.*, “Seeing around street corners: Non-line-of-sight detection and tracking in-the-wild using Doppler radar,” in *Proc. IEEE/CVF Conf. Comput. Vis. Pattern Recognit. (CVPR)*, 2020, pp. 2065–2074.

[19] B. Liu, X. Tang, R. Tharmarasa, T. Kirubarajan, R. Jassemi, and S. Hallé, “Underwater target tracking in uncertain multipath ocean environments,” *IEEE Trans. Aerosp. Electron. Syst.*, vol. 56, no. 6, pp. 4899–4915, Dec. 2020.

[20] B. Habtemariam, R. Tharmarasa, T. Thayaparan, M. Mallick, and T. Kirubarajan, “A multiple-detection joint probabilistic data association filter,” *IEEE J. Sel. Topics Signal Process.*, vol. 7, no. 3, pp. 461–471, Jun. 2013.

[21] T. Sathyam, T.-J. Chin, S. Arulampalam, and D. Suter, “A multiple hypothesis tracker for multitarget tracking with multiple simultaneous measurements,” *IEEE J. Sel. Topics Signal Process.*, vol. 7, no. 3, pp. 448–460, Jun. 2013.

[22] B. Yang, J. Wang, W. Wang, and S. Wei, “Multipath generalized labeled multi-Bernoulli filter,” in *Proc. 21st Int. Conf. Inf. Fusion (FUSION)*, 2018, pp. 1423–1429.

[23] L. Wang, S. Giebenhain, C. Anklam, and B. Goldluecke, “Radar ghost target detection via multimodal transformers,” *IEEE Robot. Autom. Lett.*, vol. 6, no. 4, pp. 7758–7765, Oct. 2021.

[24] R. Feng, E. De Greef, M. Rykunov, S. Pollin, A. Bourdoux, and H. Sahli, “Multipath ghost recognition and joint target tracking with wall estimation for indoor MIMO radar,” *IEEE Trans. Radar Syst.*, vol. 2, pp. 154–164, Jan. 2024.

[25] B. Liu, R. Tharmarasa, R. Jassemi, D. Brown, and T. Kirubarajan, “Extended target tracking with multipath detections, terrain-constrained motion model and clutter,” *IEEE Trans. Intell. Transp. Syst.*, vol. 22, no. 11, pp. 7056–7072, Nov. 2021.

[26] X. Shen, Z. Song, H. Fan, and Q. Fu, “RFS-based extended target multipath tracking algorithm,” *IET Radar, Sonar & Navigation*, vol. 11, no. 7, pp. 1031–1040, Jul. 2017.

[27] B. Liu, R. Tharmarasa, R. Jassemi, D. Brown, and T. Kirubarajan, “RFS-based multiple extended target tracking with resolved multipath detections in clutter,” *IEEE Trans. Intell. Transp. Syst.*, vol. 24, no. 10, pp. 10400–10409, Oct. 2023.

[28] C. Lundquist, K. Granström, and U. Orguner, “An extended target CPHD filter and a gamma Gaussian inverse Wishart implementation,” *IEEE J. Sel. Topics Signal Process.*, vol. 7, no. 3, pp. 472–483, Jun. 2013.

[29] M. Beard, S. Reuter, K. Granström, B. T. Vo, B. N. Vo, and A. Scheel, “Multiple extended target tracking with labeled random finite sets,” *IEEE Trans. Signal Process.*, vol. 64, no. 7, pp. 1638–1653, Apr. 2016.

[30] J. Lan and X. R. Li, “Tracking of extended object or target group using random matrix – Part I: New model and approach,” in *Proc. 15th Int. Conf. Inf. Fusion (FUSION)*, 2012, pp. 2177–2184.

[31] B.-N. Vo, B.-T. Vo, T. T. D. Nguyen, and C. Shim, “An overview of multi-object estimation via labeled random finite set,” *IEEE Trans. Signal Process.*, vol. 72, pp. 4888–4917, Oct. 2024.

[32] B.-T. Vo and B.-N. Vo, “Labeled random finite sets and multi-object conjugate priors,” *IEEE Trans. Signal Process.*, vol. 61, no. 13, pp. 3460–3475, Jul. 2013.

[33] —, “A random finite set conjugate prior and application to multi-target tracking,” in *7th International Conference on Intelligent Sensors, Sensor Networks and Information Processing (ISSNIP)*, 2011, pp. 431–436.

[34] H. Deusch, S. Reuter, and K. Dietmayer, “The labeled multi-Bernoulli filter,” *IEEE Trans. Signal Process.*, vol. 62, no. 12, pp. 3246–3260, Jun. 2014.

[35] T. T. D. Nguyen, B.-N. Vo, B.-T. Vo, D. Y. Kim, and Y. S. Choi, “Tracking cells and their lineages via labeled random finite sets,” *IEEE Trans. Signal Process.*, vol. 69, pp. 5611–5626, Sep. 2021.

[36] B.-N. Vo, B.-T. Vo, and H. G. Hoang, “An efficient implementation of the generalized labeled multi-Bernoulli filter,” *IEEE Trans. Signal Process.*, vol. 65, no. 8, pp. 1975–1987, Apr. 2017.

[37] J. Lan and X. R. Li, “Extended-object or group-target tracking using random matrix with nonlinear measurements,” *IEEE Trans. Signal Process.*, vol. 67, no. 19, pp. 5130–5142, Oct. 2019.

[38] X. Li and V. Jilkov, “Survey of maneuvering target tracking. Part I: Dynamic models,” *IEEE Trans. Aerosp. Electron. Syst.*, vol. 39, no. 4, pp. 1333–1364, Oct. 2003.

[39] K. Granstrom and U. Orguner, “New prediction for extended targets with random matrices,” *IEEE Trans. Aerosp. Electron. Syst.*, vol. 50, no. 2, pp. 1577–1589, Apr. 2014.

[40] K. Gilholm and D. Salmond, “Spatial distribution model for tracking extended objects,” *IEE Proceedings - Radar, Sonar and Navigation*, vol. 152, no. 5, pp. 364–371, Oct. 2005.

[41] K. Granstrom and U. Orguner, “Estimation and maintenance of measurement rates for multiple extended target tracking,” in *Proc. 15th Int. Conf. Inf. Fusion (FUSION)*, 2012, pp. 2170–2176.

[42] —, “A PHD filter for tracking multiple extended targets using random matrices,” *IEEE Trans. Signal Process.*, vol. 60, no. 11, pp. 5657–5671, Nov. 2012.

[43] P. Borjesson and C.-E. Sundberg, “Simple approximations of the error function Q(x) for communications applications,” *IEEE Trans. Commun.*, vol. 27, no. 3, pp. 639–643, Mar. 1979.

[44] J. Elfring, E. Torta, and R. Van De Molengraft, “Particle filters: A hands-on tutorial,” *Sensors*, vol. 21, no. 2, Jan. 2021, Art. no. 438.

[45] J. Wang, B. Yang, W. Wang, and Y. Bi, “Multiple-detection multi-target tracking with labelled random finite sets and efficient implementations,” *IET Radar, Sonar & Navigation*, vol. 13, no. 2, pp. 272–282, Feb. 2019.

[46] M. Miller, H. Stone, and I. Cox, “Optimizing Murty’s ranked assignment method,” *IEEE Trans. Aerosp. Electron. Syst.*, vol. 33, no. 3, pp. 851–862, Jul. 1997.

[47] K. Khan, S. U. Rehman, K. Aziz, S. Fong, and S. Sarasvady, “DBSCAN: Past, present and future,” in *Proc. 5th Int. Conf. Appl. Digit. Inf. Web Technol. (ICADIWT)*, 2014, pp. 232–238.

[48] J. Illingworth and J. Kittler, “A survey of the Hough transform,” *Computer Vision, Graphics, and Image Processing*, vol. 44, no. 1, pp. 87–116, Oct. 1988.

[49] S. Lin, B. T. Vo, and S. E. Nordholm, “Measurement driven birth model for the generalized labeled multi-Bernoulli filter,” in *Proc. Int. Conf. Control Automat. Inf. Sci. (ICCAIS)*, 2016, pp. 94–99.

[50] M. Beard, B. T. Vo, and B.-N. Vo, “OSPA⁽²⁾: Using the OSPA metric to evaluate multi-target tracking performance,” in *Proc. Int. Conf. Control Automat. Inf. Sci. (ICCAIS)*, 2017, pp. 86–91.

[51] K. Bernardin and R. Stiefelhagen, “Evaluating multiple object tracking performance: The CLEAR MOT metrics,” *EURASIP Journal on Image and Video Processing*, vol. 2008, May 2008, Art. no. 246309.

[52] J. Luiten *et al.*, “HOTA: A higher order metric for evaluating multi-object tracking,” *Int. J. Comput. Vision*, vol. 129, no. 2, p. 548–578, Feb. 2021.

[53] F. Kraus, N. Scheiner, W. Ritter, and K. Dietmayer, “The radar ghost dataset – An evaluation of ghost objects in automotive radar data,” in *Proc. IEEE/RSJ Int. Conf. Intell. Robots Syst. (IROS)*, 2021, pp. 8570–8577.

Guanhua Ding (Student Member, IEEE) received the B.S. and M.Sc. degrees from Beihang University (BUAA), Beijing, China, in 2020 and 2023, respectively. He is currently pursuing the Ph.D. degree in signal and information processing with the School of Electronic Information Engineering, BUAA, Beijing, China. His research interests include multi-object tracking, extended object tracking, multi-sensor data fusion, and random finite set theory.



Tao Huang (Senior Member, IEEE) received his Ph.D. in Electrical Engineering from the University of New South Wales, Australia, in 2016. Dr. Huang is a Senior Lecturer at James Cook University (JCU), Cairns, Australia. He is the Head of the International Partnerships in the College of Science and Engineering, Deputy Director of the Centre for AI and Data Science Innovation, and the Director of the Intelligent Computing and Communications Lab. He was an Endeavour Australia Cheung Kong Research Fellow, a visiting scholar at The Chinese University of Hong Kong, a research associate at the University of New South Wales, and a postdoctoral research fellow at James Cook University. Before academia, Dr. Huang was a senior engineer, senior data scientist, project team lead, and technical lead. Dr. Huang has received the Best Paper Award from the IEEE WCNC, the IEEE Access Outstanding Associate Editor of 2023 and 2024, and the IEEE Outstanding Leadership Award. He is an Associate Editor of Scientific Reports (Nature Portfolio), IEEE Open Journal of Communications Society, IEEE Access, and IET Communications. His research interests include deep learning, intelligent sensing, computer vision, pattern recognition, wireless communications, system optimization, electronics systems, and IoT security.





Qinchen Wu (Student Member, IEEE) received the B.S. and M.Sc. degrees from Beihang University (BUAA), Beijing, China, in 2019 and 2021, respectively. He is currently working toward the Ph.D. degree in signal and information processing with the School of Electronic Information Engineering, Beihang University, Beijing, China. His research interests include random finite set, group target tracking, and multi-sensor data fusion.



Guoqiang Mao (Fellow, IEEE) is a Chair Professor and the Director of the Center for Smart Driving and Intelligent Transportation Systems, Southeast University. From 2014 to 2019, he was a Leading Professor, the Founding Director of the Research Institute of Smart Transportation, and the Vice-Director of the ISN State Key Laboratory, Xidian University. Before that, he was with the University of Technology Sydney and The University of Sydney. He has published 300 papers in international conferences and journals that have been cited more

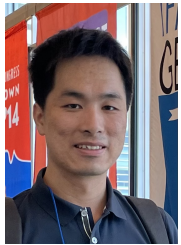
than 15,000 times. His H-index is 57 and was in the list of Top 2% most-cited scientists worldwide by Stanford University in 2022, 2023, and 2024 both by Single Year and by Career Impact. His research interests include intelligent transport systems, the Internet of Things, wireless localization techniques, mobile communication systems, and applied graph theory and its applications in telecommunications. He is a fellow of AAIA and IET. He received the “Top Editor” Award for outstanding contributions to IEEE Transactions on Vehicular Technology in 2011, 2014, and 2015. He has served as the chair, the co-chair, and a TPC member in several international conferences. He has been serving as the Vice-Director of Smart Transportation Information Engineering Society and Chinese Institute of Electronics since 2022. He was the Co-Chair of the IEEE ITS Technical Committee on Communication Networks from 2014 to 2017. He is an Editor of IEEE Transactions on Intelligent Transportation Systems (since 2018), IEEE Transactions on Wireless Communications (2014–2019), and IEEE Transactions on Vehicular Technology (2010–2020).



Jinping Sun (Member, IEEE) received the M.Sc. and Ph.D. degrees from Beihang University (BUAA), Beijing, China, in 1998 and 2001, respectively. Currently, he is a Professor with the School of Electronic Information Engineering, BUAA. His research interests include statistical signal processing, high-resolution radar signal processing, target tracking, image understanding, and robust beamforming.



Yanping Wang (Member, IEEE) received the B.S. and M.S. degrees in mechanical electronics engineering from the Beijing Institute of Technology, Beijing, China, in 1998 and 2001, respectively, and the Ph.D. degree in signal and information processing from the Institute of Electronics, Chinese Academy of Sciences, Beijing, in 2004. He is currently a Professor with the North China University of Technology, Beijing. His research interests include information fusion, ground-based radar imaging and deformation monitoring.



Bing Zhu (Senior Member, IEEE) received the B.S. and Ph.D. degrees in control theory and applications from Beihang University, Beijing, China, in 2007 and 2013, respectively. He was with University of Pretoria, Pretoria, South Africa, as a Postdoctoral Fellow supported by Vice-Chancellor Postdoctoral Fellowship from 2013 to 2015. He was with Nanyang Technological University, Singapore, as a Research Fellow from 2015 to 2016. He joined Beihang University, as an Associate Professor in 2016. His research interests include model predictive

control, smart sensing, and demand-side management for new energy systems. Dr Zhu serves as an Associate Editor for Acta Automatica Sinica.